



## 저작자표시-비영리-변경금지 2.0 대한민국

이용자는 아래의 조건을 따르는 경우에 한하여 자유롭게

- 이 저작물을 복제, 배포, 전송, 전시, 공연 및 방송할 수 있습니다.

다음과 같은 조건을 따라야 합니다:



저작자표시. 귀하는 원저작자를 표시하여야 합니다.



비영리. 귀하는 이 저작물을 영리 목적으로 이용할 수 없습니다.



변경금지. 귀하는 이 저작물을 개작, 변형 또는 가공할 수 없습니다.

- 귀하는, 이 저작물의 재이용이나 배포의 경우, 이 저작물에 적용된 이용허락조건을 명확하게 나타내어야 합니다.
- 저작권자로부터 별도의 허가를 받으면 이러한 조건들은 적용되지 않습니다.

저작권법에 따른 이용자의 권리는 위의 내용에 의하여 영향을 받지 않습니다.

이것은 [이용허락규약\(Legal Code\)](#)을 이해하기 쉽게 요약한 것입니다.

[Disclaimer](#)

이학박사학위논문

**Analgesic effect of mycolactone in  
pathological pain and characterization  
of trigeminal motor pathology in  
Alzheimer's disease**

병리학적 통증에 대한 마이코락톤의  
진통효과 및 알츠하이머병에서의  
삼차신경 운동 병리의 특성에 대한 연구

2021 년 2 월

서울대학교 대학원

자연과학대학 뇌인지과학과 전공

김 한 별

병리학적 통증에 대한 마이코락톤의 진통효과  
및 알츠하이머병에서의 삼차신경 운동 병리의  
특성에 대한 연구

지도교수 오 석 배

이 논문을 이학박사 학위논문으로 제출함

2020년 12월

서울대학교 대학원

뇌인지과학과

김 한 별

김한별의 박사학위논문을 인준함

2020년 12월

위 원 장	목 인 희	(인)
부 위 원 장	오 석 배	(인)
위 원	이 인 아	(인)
위 원	류 현 모	(인)
위 원	정 민 환	(인)

**Analgesic effect of mycolactone in pathological  
pain and characterization of trigeminal motor  
pathology in Alzheimer's disease**

Advisor: Prof. Seog Bae Oh, D.D.S, Ph.D

A dissertation submitted in partial fulfillment  
of the requirement for the degree of

**DOCTOR OF PHILOSOPHY**

to the faculty of the

**Department of Brain and Cognitive Science**

at

**SEOUL NATIONAL UNIVERSITY**

by

**Han Byul Kim**

**Date approved:**

December, 2020

문 인 희 Duhue

Seog Bae OH

이 인 아

Hyun-Mo RYOO

Min Whan Jung

# **ABSTRACT**

## **Analgesic effect of mycolactone in pathological pain and characterization of trigeminal motor pathology in Alzheimer's disease**

**Han Byul Kim**

Sensory and motor functions play an important role in maintaining physiological functions of the body. Neurological disorders are defined as disorders that affect the central and peripheral nervous system. As sensory and motor abnormalities are commonly manifested in neurological disorders, it can result in a range of symptoms. Examples of these symptoms can be divided into neurological symptoms such as altered levels of consciousness, seizures and confusion and motor dysfunctions such as paralysis, muscle weakness and poor coordination, as well as sensory dysfunctions such as loss of sensation and pain. To gain understanding on the mechanisms of sensory abnormalities induced by neurological disorders such as neurological pain caused by inflammation or nerve damage, and further validate analgesic effect of potential candidate for novel analgesic compound, I investigated the analgesic property of mycolactone, a bacteria-derived toxin which causes non-painful ulcers. Furthermore, to gain understanding on the mechanisms of motor abnormality, specifically masticatory

dysfunction as found in Alzheimer's disease (AD), I investigated the cranial nuclei innervating orofacial regions and masticatory muscles in 5XFAD mice as below.

In the first chapter, I assessed the analgesic properties of mycolactone on behavioral models and nociceptive neurons. I first investigated the analgesic property of mycolactone *in vivo* via acute inflammatory pain model induced by 1% formalin. The thickness of the mycolactone injected hind paw showed significantly less inflammation, as well as, analgesia in nocifensive behavior from the second phase of formalin test. For the investigation of analgesic effect of mycolactone on neuropathic pain, I used the chronic constriction injury (CCI) model. The analgesic effect of mycolactone was found in mechanical threshold after i.t. injection of 5 $\mu$ M mycolactone in a dose-dependent manner. The effective dose of mycolactone (5 $\mu$ M) also showed an analgesic effect in the Hargreaves test. Furthermore, to investigate possible mechanism of analgesic property of mycolactone *in vitro*, I developed a dedicated medium-throughput cellular assay based on membrane potential changes, using bis-oxonol-voltage sensitive dye loaded Dorsal Root Ganglion (DRG) neurons. I demonstrated that mycolactone at non-cytotoxic doses triggers the hyperpolarization of DRG neurons through AT2R, with this action being unaffected by known ligands of AT2R. Altogether, these results indicate an analgesic property of mycolactone and a possible underlying mechanism through AT2R-dependent signaling pathways in DRG neurons with the potential for development of novel nature-inspired analgesics.

In the second chapter, I have assessed masticatory behavior and pathological hallmarks of AD in 5XFAD mouse. 5XFAD mice showed a

decreased masticatory efficiency and maximum biting force, while there was no significant change in general motor function. Moreover, significant accumulation of amyloid- $\beta$  (A $\beta$ ), increased number of active microglia, and cell death in trigeminal motor nucleus (Vmo) were observed compared to other mastication-related nucleuses. Furthermore, mastication-related tissues were histologically analyzed and showed a decreased masseter muscle volume and muscle fiber diameter compared to other facial or hypoglossal nuclei innervating muscles. Taken together, the results suggest that degeneration of masticatory function may be involved in progression of AD and control of masticatory function could potentially benefit the control of AD symptoms.

Following results from chapter I and chapter II suggest that targeting peripheral abnormalities found in neurological disorders such as pathological pain (chapter I) can provide insight on potential use of bacteria derived molecule for treatment intervention. Also, for the central neurological disorder such as AD (chapter II), the outcome of this research proposes the importance of understanding the link between trigeminal motor system and manifestation of masticatory dysfunction found in AD. Thus, altogether, this paper underlies the importance of investigating peripheral sensory-motor abnormalities in understanding of peripheral and central neurological disorders.

---

Key Words: Mycolactone; AT2 receptors; DRG neurons; membrane potential; image-based assay; pain; Alzheimer's disease; Mastication; 5XFAD

---

Student Number: 2014-22437

# CONTENTS

Abstract.....	1
Contents.....	4
List of figures.....	5
List of tables.....	7
Background.....	8
Purpose.....	18
<b>CHAPTER 1: Mycolactone as a novel analgesic molecule.....</b>	<b>19</b>
Abstract.....	20
Introduction.....	22
Materials and methods.....	25
Results.....	35
Discussion.....	59
<b>CHAPTER 2: A<math>\beta</math> accumulation in Vmo contributes to masticatory dysfunction in 5XFAD mice.....</b>	<b>66</b>
Abstract.....	67
Introduction.....	68
Materials and methods.....	70
Results.....	75
Discussion.....	92
<b>General discussion.....</b>	<b>95</b>
<b>References.....</b>	<b>97</b>
<b>국문초록.....</b>	<b>103</b>



# LIST OF FIGURES

## Background

Figure 1. Functional Classes of Neurons.....	34
Figure 2. Graphical illustration of afferent pain pathways as drug targets for and analgesic drugs.....	34
Figure 3. Pain management and side effects.....	34
Figure 4. Graphical illustration of amyloid- $\beta$ (A $\beta$ ) plaque formation in Alzheimer disease.....	34
Figure 5. Graphical illustration of questions from each chapter.....	34

## Chapter 1

Figure 6. Mycolactone induced analgesia in mouse chronic constriction injury model.....	34
Figure 7. Morphology of the Dorsal Root Ganglion (DRG) neurons 3 days after harvesting in 384-well microplates.....	36
Figure 8. Stability of DiSBAC2 (3) intensity in DRG neurons.....	38
Figure 9. Change in membrane potential in DRG neurons.....	40
Figure 10. Time dependence of the effect of mycolactone on the viability of DRG neurons.....	42
Figure 11. Characterization of the effects of mycolactone on DRG neurons. .....	57
Figure 12. Effect of high affinity ligands to AT2R on DRG neurons.....	59
Figure 13. Schematic overview of dorsal root ganglion (DRG) culture and DiSBAC2 (3) assay in a micro-titer plate.....	61

## **Chapter 2**

<b>Figure 14. Measurement of masticatory efficiency in 5XFAD mice.....</b>	<b>78</b>
<b>Figure 15. A<math>\beta</math> accumulation in cranial motor nuclei of 5XFAD mice.....</b>	<b>80</b>
<b>Figure 16. A<math>\beta</math> accumulation in ventromedial and dorsolateral division of cranial motor nuclei of 5XFAD mice.....</b>	<b>82</b>
<b>Figure 17. Brain inflammation and cell death in the cranial motor nuclei of 5XFAD mice.....</b>	<b>84</b>
<b>Figure 18. Histological characterization of masseter muscle in 5XFAD mice. .....</b>	<b>84</b>
<b>Figure 19. Histological analysis of the digastric muscle and hyoglossus muscle of 5XFAD mice.....</b>	<b>84</b>
<b>Figure 20. Volumetric analysis of the mouse first molar in 5XFAD mice..</b>	<b>86</b>

## LIST OF TABLES

<b>Table 1. Cytotoxicity induced by mycolactone in different cell types.</b>	<b>34</b>
<b>Table 2. Ligand binding affinities to AT2R.</b>	<b>36</b>

# BACKGROUND

Based upon the direction of the signal relay, neurons can be functionally classified into three types; sensory, motor and interneurons (Martini 2006). In the peripheral nerve ending, physical stimuli, such as temperature touch and nociception are transduced into action potentials, which then transmitted to the spinal cord or brain. Sensory neurons are also referred to as afferent neurons, as they relay stimulus information to the central nervous system (**Fig. 1A**). Motor neurons are called efferent neurons which transmit neural signals from the brain and spinal cord to the muscles (**Fig. 1B**). Interneurons modulate nerve impulses within the central nervous system and are exclusively confined to the central nervous system. (**Fig. 1C**). Abnormalities found in sensory and motor neurons often cause functional deterioration in the peripheral system. Therefore, understanding the basis of neurological disorders are crucial in developing the modulatory means for such abnormalities. Neurological disorders are defined as disorders that affect the central and peripheral nervous system. The pathological conditions that disrupt the biophysical function of sensory and motor neurons can result in development of neurological disorders. Pathological conditions of the nervous system can result in a range of symptoms. Examples of these symptoms include altered levels of consciousness, seizures, confusion. Moreover, motor dysfunctions such as paralysis, muscle weakness and poor coordination, as well as sensory dysfunctions such as loss of sensation and pain can be manifested as the primary symptoms. Examples of these disorders diagnosed from these symptoms may include sensory abnormality such as pain and neurodegenerative disease such as Alzheimer's disease (Borsook 2012).

Sensory abnormality such as pain is perceived by afferent pain pathways

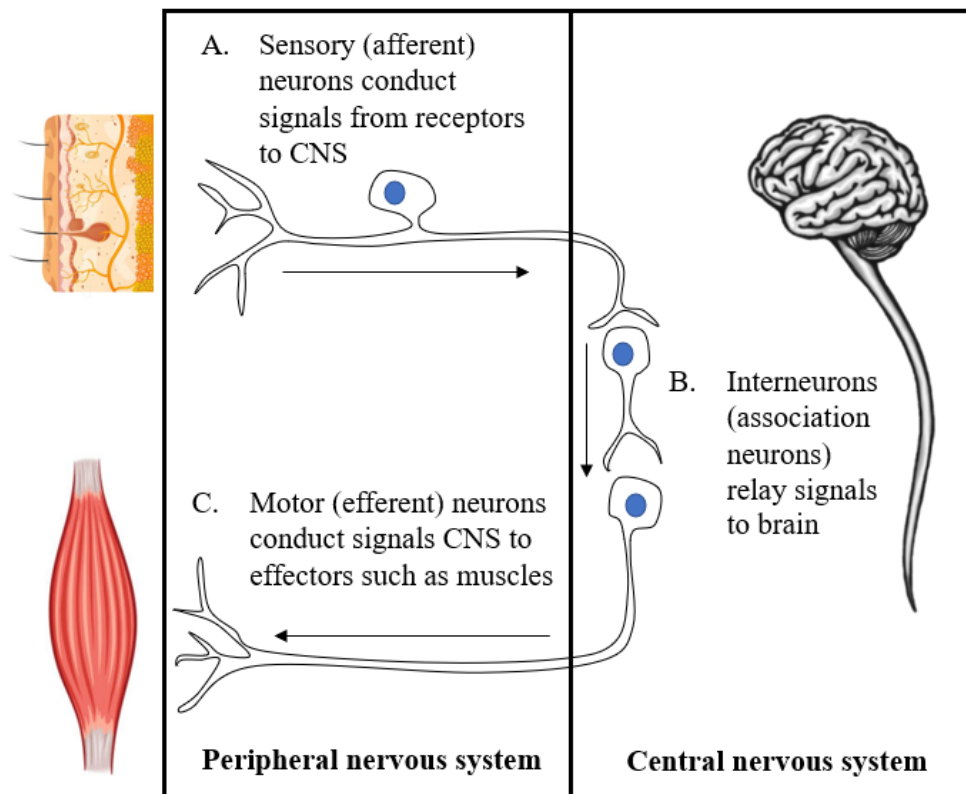
which have four main processes: transduction, transmission, modulation and perception (**Fig. 2**) (Salat et al. 2013). Transduction is a process in which potentially noxious stimuli such as chemical signals are converted to electrical signals by nociceptors present at the site of the tissue damage (Woolf 2004). Activation of these nociceptors then generates action potentials and the noxious signals are transmitted through afferent sensory nerve fibers such as A $\delta$  fibers which transmit ‘fast’ pain, and C fibers which transmit ‘slow’ pain (Farquhar-Smith 2008). These signals are transmitted to the spinal dorsal horn and relayed to the thalamus and somatosensory cortex of the brain for perception. While noxious signals are relayed to the brain, these signals can be modulated in both peripheral and central sites. Traditionally for the management of pain, depending on the severity of the pain (**Fig. 3A**) (Hylands-White et al. 2017) and the site of action (**Fig. 2**) (Salat et al. 2013), different stages of afferent pain pathways are targeted by a range of drugs. Local anesthetics such as sodium channel blocker or potassium channel agonists, TRP channel antagonists and anti-inflammatory drugs are used to block transduction and transmission, while, opioids and  $\alpha 2$  agonists are used to block transmission in central nervous system (Juárez-Contreras et al. 2018). Although a set of therapeutic guidelines for the administrative use of analgesics are present, currently available analgesics are limited in their efficacy as they are often unable to fully manage pain in patients (Krames 1999). Moreover, strong opioids such as morphine, fentanyl and methadone often have side effects such as drowsiness, impaired coordination, nausea and vomiting (**Fig. 3B**) (Nicholas 2019). These indicate that development of novel analgesics with greater efficacy and less side effects are crucial. For compound screening and hit selection for potentially targeted drugs, it is important to set up phenotypic cellular assays (Feng et al. 2009; Moffat et al.

2017). Depending on molecular and functional phenotypes shown by the target disorders, it is essential to set the appropriate parameters for phenotypic cellular assays to screen or monitor drug effect. For example, for the development of novel analgesics, change in membrane voltage can be detected by voltage-sensing dyes to visualize the hyperpolarization induced by potential analgesic molecules which indicate that hyperpolarization can be set as the parameter for monitoring drug effect. Recently researchers successfully used bacteria derived natural products such as Botox for pain management (Royal 2003). Concomitantly, another bacteria derived key molecule such as mycolactone is examined for their potential analgesic properties (Marion et al. 2014).

Given that the direct modulation of sensory pathways is essential for development of pain therapeutics, it is also valuable to find and validate the target for functional deterioration of the peripheral system caused by neurodegenerative diseases such as Alzheimer's disease (AD) for its therapeutic intervention. Alzheimer's disease is one of the most common causes of dementia resulting from progressive degeneration of the central nervous system (Rosen et al. 1984). AD is generally thought to result from neuronal death caused by the accumulation of amyloid  $\beta$  ( $A\beta$ ) protein.  $A\beta$ , the neurotoxic peptide, is cleaved from amyloid precursor protein (APP) and can further aggregate to form  $A\beta$  plaques (**Fig. 4**) (Panza et al. 2019). Brain imaging of AD patients has revealed degeneration of symptom-related brain regions such as entorhinal cortex and hippocampus, which is responsible for memory and navigation deterioration (Johnson et al. 2012). Apart from cognitive deterioration, accumulation of  $A\beta$  is also closely related to sensory and motor dysfunctions such as vision, olfaction, and gait problems seen in AD patients (Frost et al. 2010; He et al. 2018; Lewis et al. 2006;

Mesholam et al. 1998; O'Keeffe et al. 1996). Recent clinical research has indicated sensory and motor dysfunctions to be precedent as early as 15 years to cognitive decline (Albers et al. 2015). Therefore, sensory and motor abnormalities are intensively studied in AD to establish the parameters for the progression and severity of the disease in early diagnosis. Additionally, recent studies have found a significant cognitive decline in AD patients with oral impairments and masticatory malfunctions such as oral dyskinesia, periodontitis, and tooth loss (Campos et al. 2017; Singhrao et al. 2014). Specific sites for A $\beta$  accumulation have yet to be addressed in the orofacial sensorimotor system despite the correlation observed in oral dysfunction and cognitive impairment (Campos et al. 2017; Onozuka et al. 2000).

**Figure 1.**



**Functional Classes of Neurons.** (A) Sensory (afferent) neurons carry signals to the central nervous system (CNS); (B) interneurons are contained entirely within the CNS and relay signals to the brain; and (C) motor (efferent) neurons carry signals from the CNS to muscles.

**Fig 1.** Adopted and modified from (Martini 2006)



**Figure 2.**

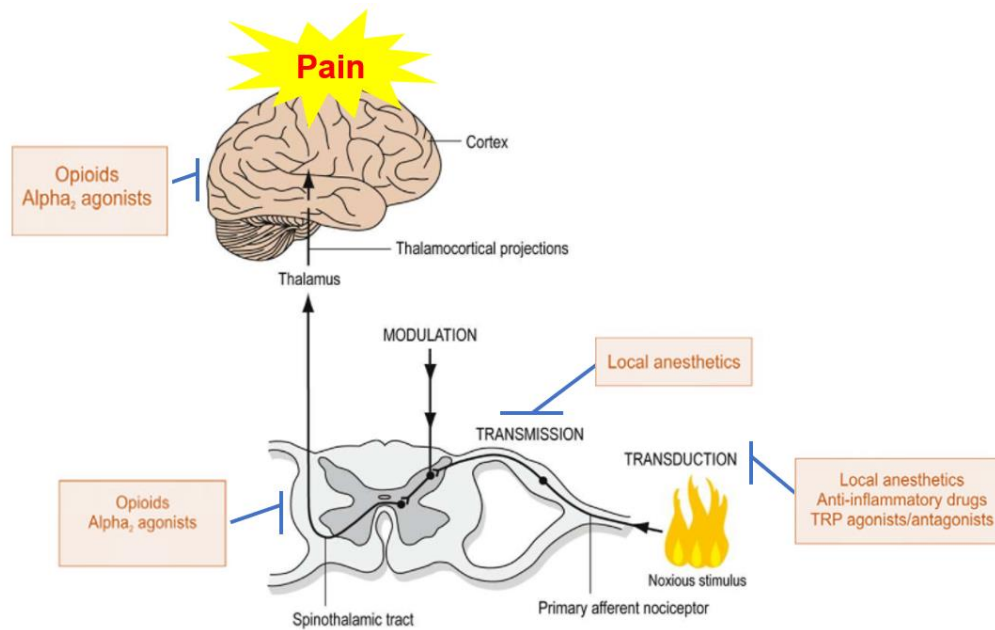
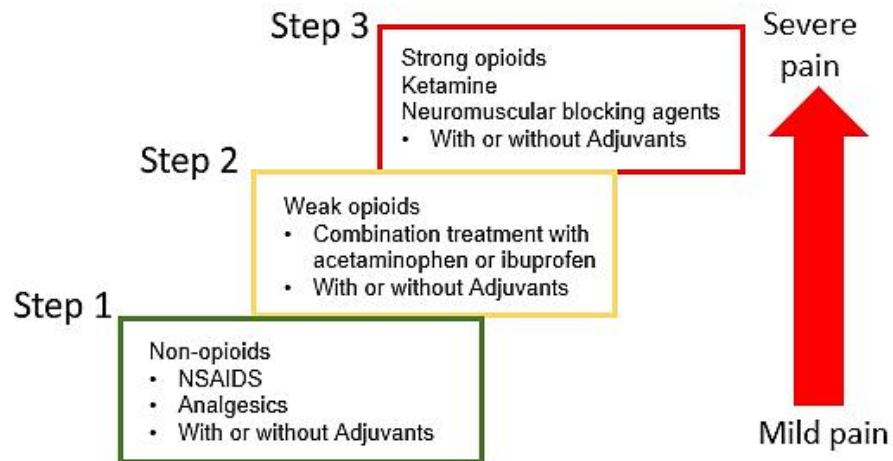


**Figure 2. Graphical illustration of afferent pain pathways as drug targets for and analgesic drugs**

**Fig. 2** Adopted and modified from (Salat et al. 2013)

**Figure 3**

**A**



**B**

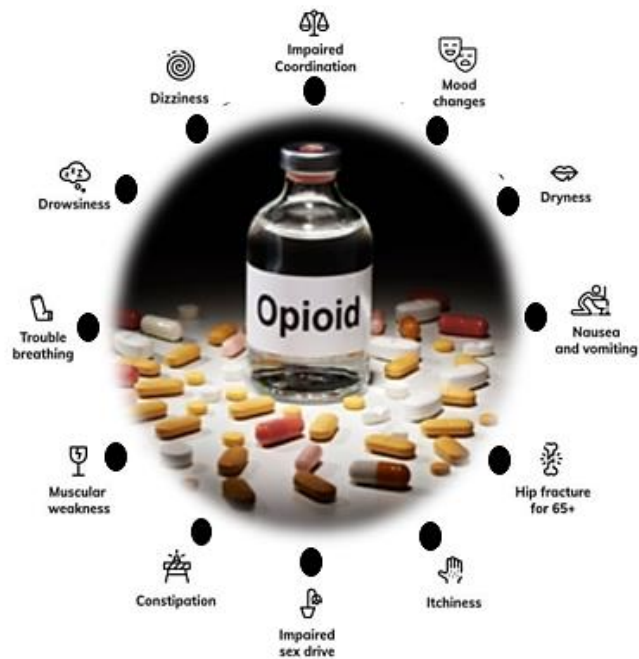


**Figure 3. Pain management and side effects** (A) Three-step WHO pain ladder divided by intensity of the pain and use of opioids. (B) Diverse side-effects of opioids

**Fig. 3A** Adopted and modified from (Hylands-White et al. 2017)

**Fig. 3B** Adopted and modified from (Nicholas 2019)

## Figure 4

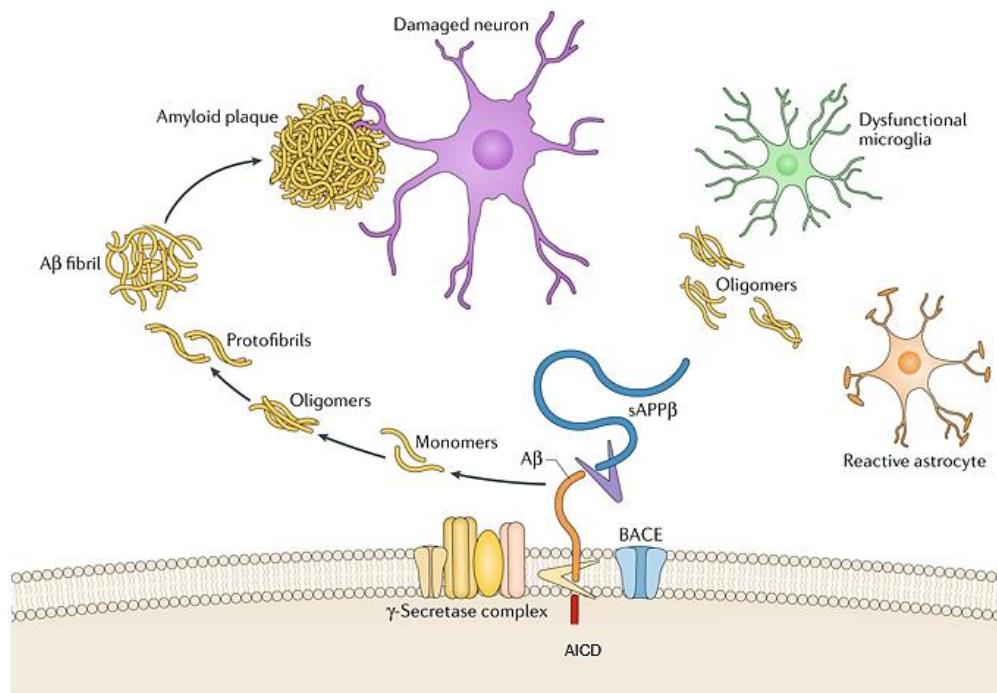


**Figure 4. Graphical illustration of amyloid- $\beta$  (A $\beta$ ) plaque formation in Alzheimer disease.** AICD, amyloid precursor protein intracellular domain; BACE,  $\beta$ -secretase; sAPP $\beta$ , soluble amyloid precursor protein- $\beta$ .

**Fig 4.** Adopted and modified from (Panza et al. 2019)

**Figure 5**

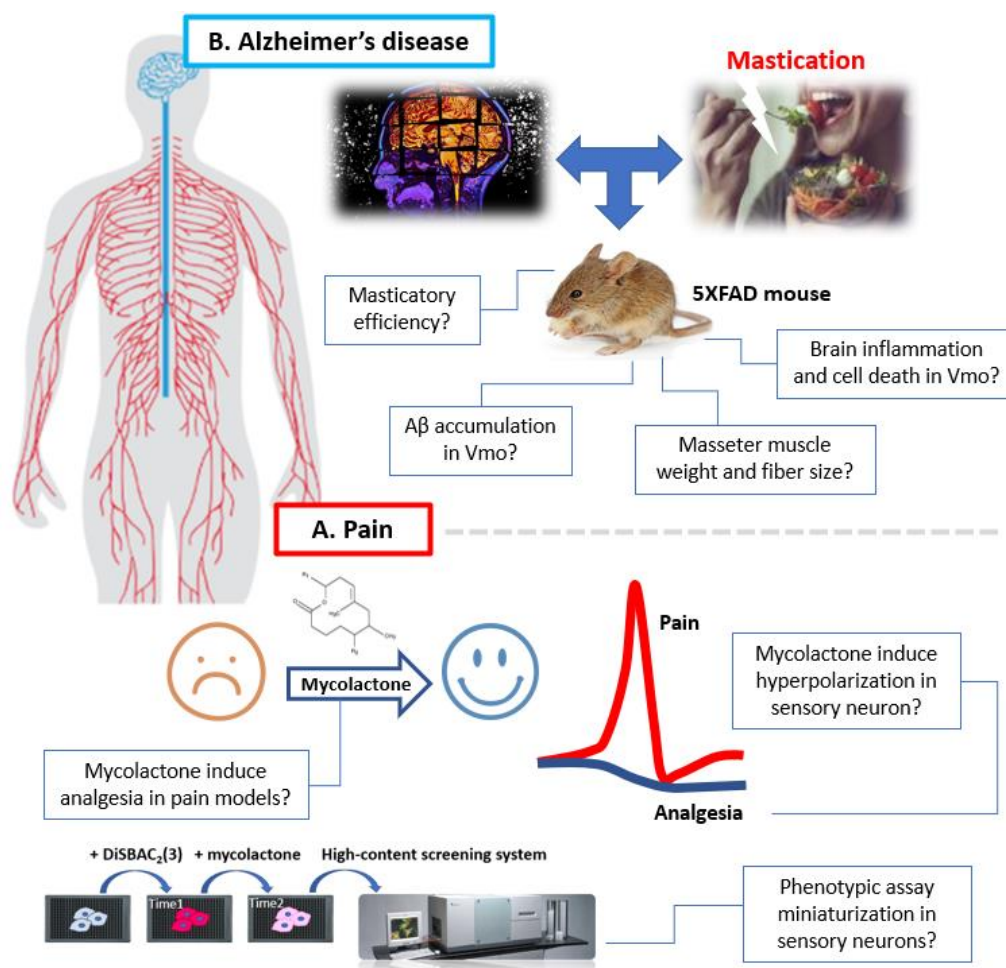


**Figure 5. Graphical illustration of questions from each chapter. (A) Chapter I and (B) Chapter II.**

# PURPOSE

The efficacy of currently available analgesics such as NSAIDS and opioids is limited in the treatment of sensory abnormalities as found in neuropathic pain. In an attempt to develop novel analgesics through investigation of *M.ulcerans* derived natural toxin, Mycolactone, I have first attempted to demonstrate the analgesic effect of mycolactone *in vivo*. Then I have focused on development of a medium-throughput phenotypic cellular assay to test hyperpolarization induced by mycolactone and validate the mode of action of mycolactone induced hyperpolarization (**Fig 5. A**). Moreover, in an attempt to find and validate the target for functional deterioration of peripheral system caused by neurodegenerative disease such as Alzheimer's disease, I have focused on identification of A $\beta$  pathology in cranial nuclei innervating orofacial regions and investigation of following behavioral and histological outcomes to understand the relationship between Alzheimer's disease and masticatory dysfunction found in AD patients (**Fig 5. B**).

- To confirm mycolactone-induced analgesia *in vivo*.
- To develop the phenotypic cellular assay using sensory neuron to confirm the analgesic pathway of mycolactone *in vitro*.
- To examine whether specific A $\beta$  pathology affects the masticatory system in 5XFAD mice, focusing on examining histological differences of cranial nuclei innervating orofacial region for A $\beta$  accumulation and comparing peripheral components of masticatory system.

# **CHAPTER 1:**

## **Mycolactone as a novel analgesic molecule**

*\*This chapter has been largely reproduced from articles published by Song, O. R., Kim, H. B., Jouny, S., Ricard, I., Vandeputte, A., Deboosere, N., ... & Henrion, D. (2017). A bacterial toxin with analgesic properties: hyperpolarization of DRG neurons by mycolactone. Toxins, 9(7), 227.*

## ABSTRACT

Mycolactone, a polyketide molecule produced by *Mycobacterium ulcerans*, is the etiological agent of Buruli ulcer. This lipid toxin is endowed with pleiotropic effects, presents cytotoxic effects at high doses, and notably plays a pivotal role in host response upon colonization by the bacillus. Most remarkably, mycolactone displays intriguing analgesic capabilities: the toxin suppresses or alleviates the pain of the skin lesions it inflicts. Previously it was demonstrated that the analgesic capability of mycolactone was not attributable to nerve damage, but instead resulted from the triggering of a cellular pathway targeting AT2 receptors (angiotensin II type 2 receptors; AT2R), and leading to potassium-dependent hyperpolarization. This demonstration paves the way to a new nature-inspired analgesic compound. In this direction, I first induced an acute inflammatory pain model to test the analgesic property of mycolactone in various pain models. The intraplantar injection of 1% formalin on right hind paw elicited nocifensive responses such as flinching and licking and this was recorded for 40 minutes. The thickness of the right hind paw was also measured 2 hours post injection. The result showed significantly less inflammation of the paw treated with mycolactone as well as significantly less nocifensive behavior in the second phase of formalin test which indicates analgesic property of mycolactone towards the acute inflammatory pain. I also used the CCI model to produce neuropathic pain in 8 weeks old adult mice. Analgesic effect of mycolactone, 0.5 and 5 $\mu$ M, was tested after intrathecal injection at 14 days after surgery, by measuring the changes of threshold in response to mechanical stimulations with a series of von Frey filaments. Mycolactone increased the mechanical threshold in 5 $\mu$ M injection but not in 0.5 $\mu$ M, thus inducing analgesia in neuropathic mice in a dose



dependent manner. The effective dose of mycolactone (5 $\mu$ M) also showed an analgesic effect in Hargreaves test. Next, I assess the hyperpolarizing properties of mycolactone on nociceptive neurons by developing a dedicated medium-throughput assay based on membrane potential changes. This was visualized by confocal microscopy of bis-oxonol-loaded Dorsal Root Ganglion (DRG) neurons. I demonstrated that mycolactone at non-cytotoxic doses triggers the hyperpolarization of DRG neurons through AT2R, with this action being not affected by known ligands of AT2R. This result points towards novel AT2R-dependent signaling pathways in DRG neurons underlying the analgesic effect of mycolactone, with the perspective for the development of new types of nature-inspired analgesics.

# INTRODUCTION

*Mycobacterium ulcerans* is the causative agent of Buruli ulcer (BU), a severe infective skin disease, which now represents the third most common mycobacterial disease in the world, after tuberculosis and leprosy (O'Brien et al. 2014; Organization 2012). This skin disease that has re-emerged in the last two decades affects mainly children, and provokes lesions that can often lead to permanent disabilities (Yotsu et al. 2015). Epidemiological studies have shown that aquatic environments represent the main reservoir of *M. ulcerans* (Marsollier et al. 2002; Meyin A Ebong et al. 2016). *M. ulcerans* is able to colonize various ecological niches, from aquatic environments to humans. Indeed, in aquatic environments, numerous aquatic vertebrates and macroinvertebrates harbor the bacilli. The exact ecology and mode(s) of transmission of *M. ulcerans* to humans need still to be fully specified. In Buruli ulcer disease, skin lesions are caused by a toxin, called mycolactone, the main virulence factor of *M. ulcerans* (George et al. 1999). As such, the secretion of this toxin represents a unique and distinctive feature characterizing *M. ulcerans*, playing a central role in its eco-epidemiology and pathogenesis (Demangel et al. 2009; Sarfo et al. 2016). After penetration in the skin, the lifecycle of *M. ulcerans* includes an intracellular phase, allowing the bacillus to evade host immune system recognition. Upon secretion of mycolactone, *M. ulcerans* enters an extracellular stage, with a massive destruction of host tissue, caused by a local increase in the concentration of the toxin. In fact, beyond its cytotoxic properties, the pleiotropic effects exerted by the toxin are observed in these two main lifecycle stages, with mycolactone modulating the immune system, influencing the production of cytokines, and acting on the peripheral nervous system, rendering the skin lesions painless

(Sarfo et al. 2016). The singularity of the analgesia exerted by mycolactone resides in the underlying signaling pathway (Marion et al. 2014). More specifically, researchers demonstrated that mycolactone induces analgesia, without nerve damage, by targeting angiotensin pathways, leading to the potassium-dependent hyperpolarization of neurons upon binding to angiotensin II type 2 receptors (AT2R). The absence of nerve damage was formally demonstrated in animal models by inoculation with mycolactone, with animals recovering their sensibility 48 h after injection. Altogether, results and observations strongly suggest that the cytotoxic and analgesic effects of mycolactone are mediated by distinct pathways. Previously, researchers demonstrated that mycolactone, targeting angiotensin pathways, is capable of triggering potassium-dependent hyperpolarization in cells of different types, including macrophages, PC12 pheochromocytoma cells, and hippocampal neurons (Marion et al. 2014). However, this study did not include nociceptive-specific cells. It is then mandatory, in the way towards the development of mycolactone-inspired analgesics, to extend the studies to this type of sensory cell. In this context, I first confirmed the analgesic effect of mycolactone in various pain models. Then I assessed the capability of mycolactone to hyperpolarize Dorsal Root Ganglion neurons (DRG neurons). Importantly, in this background, it appears that AT2R is indeed expressed in DRG neurons, as typically isolated, for in vitro studies, from the spinal cord of rats (Benitez et al. 2017), of mice (Yu et al. 2014), or from injured nerve specimens from adult humans (Anand et al. 2013). In order to conduct the study on the action of mycolactone on DRG neurons, I developed a dedicated medium-throughput assay, which allows for the monitoring of the changes of membrane potentials in a large number of DRG neurons. More specifically, this streamlined assay relies on the automated image

analysis of membrane potential changes, visualized by confocal microscopy of bis-oxonol-loaded DRG neurons. As this development, beyond the specific objective, can be valuable for its own sake for various medium-throughput assays of neuroactive compounds on DRG neurons, I first detail the methodology on general grounds, pointing out various advantages in this context as compared to the patch-clamp approach, the gold standard technique for the analysis of the electrical properties of neurons. In this respect, above all, using only a very small number of mice (typically 4–6), the medium-throughput miniaturized assay allows for studies to easily analyze more than 100 different conditions, with about 400 DRG neurons for any given condition. By comparison, with electrophysiology, studies would be typically limited to significantly lower numbers of different conditions and cells. Using the streamlined assay, I address the question of the action of mycolactone on DRG neurons. I demonstrate that, at non-cytotoxic doses, mycolactone triggers hyperpolarization of DRG neurons through AT2R. Finally, this study can be further envisioned in the more general context of the search for nature-inspired analgesic solutions. Indeed, as largely emphasized recently, such approaches appear to represent, in the search for new analgesics, promising alternatives to the traditional pharmacological strategies, whose limitations have become increasingly apparent (as well summarized by the title of an editorial review in the *Lancet* journal: “Results in Analgesia—Darwin 1, Pharma 0”) (Wood 2013). In this context, I suggest the perspectives opened by the study for the development of new analgesics inspired by the natural solution for analgesia implemented in Buruli ulcer.

# MATERIALS AND METHODS

## *Experimental Animals*

Six to eight (6–8) week-old C57bl/6 male mice were purchased from Janvier (Le Genest-Saint-Isle, France), Daehan biolink (Chungbuk, Korea) and Duyeol Korea (Gwangju, Korea). In accordance with Korean regulations, all procedures for animal use were reviewed and approved by the Institutional Animal Care and Use Committee at Seoul National University. In accordance with French regulations (Decret 2013-118—Ministerial Order of 1 February 2013, corresponding to the transposition of the European Directive (2010/063 EU)), the animal experiments were carried out in the animal facility at the Institute Pasteur of Lille. The animal experiments followed the protocol authorized by the Minister of Higher Education and Research and Institutional Animal Care and Use Committee at Seoul National University, Korea. AT2R knock-out mice were provided by Ulrich Wenzel (Hamburg)(Hein et al. 1995).

## *Formalin test*

Mice were acclimated in cages at least for a week and then adapted in an acrylic observation chamber (size ranges  $12 \times 12 \times 12$  cm) before the experiment at least three times. A mirror was located at  $45^\circ$  angle below the chamber to observe the paws. Formalin test was performed by intraplantar (i.pl.) injection of 1% formalin as previously described (Cho et al., 2006). On the day of test, mice were acclimatized for 30 minutes in an acrylic chamber and then 20  $\mu$ l of 1% formalin was injected subcutaneously into the plantar surface of the right hind paw via a 31-gauge needle using a 0.3 3-ml insulin syringe. Following formalin injection,

the animals were immediately placed in a test chamber and recorded using a video camera for a period of 40 min. The time mice spent licking or biting was measured in 5-minute intervals by an observer who was blinded to the treatment. Formalin-induced pain behaviors during 0–10 min after formalin injection represented the first phase and during 10–40 min after formalin injection represented the second phase.

### ***Chronic constriction injury (CCI) model surgery***

Adult male mice may be anaesthetized by isoflurane (3% induction; 2% maintenance) at 2 L/min in O<sub>2</sub> via a face mask. For surgery the mouse was laid on a warm pad in a prone position, then the right upper leg was shaved, iodine was treated and incision was made parallel to the femur. The quadriceps femoris muscle and the biceps femoris muscle are parted by careful dissection with blunt forceps to expose the sciatic nerve proximal to the trifurcation. Three silk sutures (7-0; Ailee Co. Ltd, Busan, Korea) are tied loosely around the full circumference of the sciatic nerve 2-3 mm apart and secured with a reef knot. Care should be taken for the sutures to lie adjacent to but not visibly compressing the nerve and intraneural blood flow should not be impeded. The wound is closed by suturing two layers; muscle fascia and skin by silk suture and autoclip. This protocol is based on the sciatic nerve CCI model in the rat (Bennett and Xie 1988).

### ***Behavioral testing***

All sensory testing was performed in an isolated room maintained at  $22 \pm 2^\circ\text{C}$  and  $50 \pm 10\%$  humidity. For mechanical threshold (von Frey filament) testing, mice were brought from the animal colony and placed in transparent plastic boxes on a metal mesh floor with 5x5 mm holes (Ugo Basile, Italy). The mice were then

habituated for at least 1 hour prior to testing. To assess mechanical sensitivity, the withdrawal threshold of the ipsilateral hind paw was measured using a series of von Frey filaments (0.20, 0.40, 0.70, 1.6, 3.9, 5.9, 9.8 and 13.7 mN, Stoelting, Wood Dale, IL, USA; equivalent in grams to 0.02, 0.04, 0.07, 0.16, 0.40, 0.60, 1.0 and 1.4). The 50% withdrawal threshold was determined using the 'up-down' method and calculated using Up-Down Reader software (Gonzalez-Cano et al., 2018). A brisk hind paw lift or flinch in response to von Frey filament stimulation was regarded as a withdrawal response. The 0.4 g filament was the first stimulus to be used, and, when a withdrawal response was obtained, the next weaker filament was used. This process was repeated until no response was obtained then the next stronger filament was administered. All behavioral testing was performed blind to the treatment groups. To test thermal hyperalgesia (Hargreaves test), mice were placed on a glass plate heated to 36°C within an acrylic container then left and right paws were exposed to the laser (Plantar Analgesia Meter, IITC, CA, USA), and the latency to flinching, licking one of the hind paws or jumping was measured. A cut-off time of 60 s was used to minimize the possibility of cutaneous tissue damage.

### ***Materials***

DMEM medium, Neurobasal A medium, F-12 medium, Fetal Bovine Serum (FBS), HBSS, D-PBS, Penicillin/Streptomycin, B-27, Collagenase II, Dispase II, Trypsin, Alexa Fluor® 647 conjugated anti-rabbit antibody, and DiSBAC2(3) were purchased from Life Technologies (Carlsbad, CA, USA). DNase 1, 30% BSA, Cytosine  $\beta$ -D-arabinofuranoside hydrochloride (ARA-c), 5-Fluoro-20 - deoxyuridine 5' -monophosphate sodium salt (FdU) solution (FdU), poly-D-Lysine, DAPI, and 10% neutral buffered formalin solution were purchased from

Sigma-Aldrich (Saint Louis, MO, USA). Angiotensin II was purchased from Tocris (Bristol, UK). C21 (MW = 475.2) and EMA401 (MW = 507.2) were synthesized by AGV discovery (Clapiers, France), purified by HPLC (>95%), and characterized by <sup>1</sup>H NMR and mass spectrometry. Anti-rabbit  $\beta$ 3-Tubulin (D71G9) XP® (anti-Tuj1) was purchased from Cell Signaling Technologies® (Danvers, MA, USA). Micro-titer plate (384-well),  $\mu$ Clear®, was purchased from Greiner Bio-One SAS (Les Ulis, France). Purified mycolactone was obtained and quantified as described in a previous study (Marion et al. 2014), and re-suspended in DMSO at 5 mg/mL and stored at -20 °C as aliquots in amber glass tubes.

#### ***Dissection and Dissociation of Mouse DRG Neurons Adult***

Mice were euthanized after isoflurane anesthesia (Aerrane®, Baxter SAS, Guyancourt, France), and the spine was removed. A vertebra was opened carefully by cutting along the frontal plane, to separate the dorsal and ventral sides. DRGs were dissected out from both sides of the spinal cord under the Stereomicroscope. The digestion of connective tissues in the DRGs was carried out for 50 min in a collagenase (380 units)/dispase (2 units) mix, followed by a 0.25% trypsin treatment for further digestion. One milliliter (1 mL) to 200  $\mu$ L pipette tips (large to small) were used to dissociate the DRG neurons into single cells. Large sized debris were stained using a 100  $\mu$ m cell strain. The remaining small sized debris and cells were centrifuged on a density gradient composed of 30% BSA solution and Ham's F-12 Nutrient Mix. Cells whose diameter was greater than 16  $\mu$ m were counted after trypan blue staining, using the Tali™ Image-Based Cytometer (Life Technologies, Carlsbad, CA, USA).



### ***Culture of DRG Neurons in 384-Well Microtiter Plates***

On day one, dissociated DRG neurons were seeded, at a density of 4000 cells per well, in a poly-D-lysine coated 384-well microtiter plate (Greiner Bio-One SAS, Les Ulis, France) using 40  $\mu$ L neurobasal A medium (supplemented with 10% heat-inactivated FBS, 2% B-27, and 1 $\times$  Penicillin/Streptomycin). On day two, 10  $\mu$ L plating medium containing ARA-c and FdU was added on the top of the cells, to a final concentration of 10  $\mu$ M ara-c and 20  $\mu$ M FdU, respectively. On day three, the medium in the wells was changed to (50  $\mu$ L) fresh plating medium, and the cells were incubated overnight.

### ***Dorsal root ganglion (DRG) culture***

Mice were sacrificed by exposure to isoflurane and decapitated. DRG were isolated in cold HBSS (Welgene, Korea) and incubated in 3 ml HBSS containing 1 mg/ml collagenase (Roche, USA) / 2.4 U/ml dispase II (Roche, USA) for 1 h at 37 °C. Then DRG were digested by 0.25% trypsin in PBS for 7 min at 37 °C, inactivated by 2 ml 0.25% trypsin inhibitor (Sigma, USA) and 2 ml DMEM containing 10% fetal bovine serum (Gibco, USA) / 1% pen strep (Gibco, USA) and washed by 4 ml DMEM (FBS / pen strep). DRG neurons were triturated using fire-polished pasteur pipette to separate cells. The cells were resuspended in neurobasal medium (Gibco, USA) containing B-27 supplement (Gibco, USA), 1% pen strep, L-glutamine (1 mM), placed on cover slips coated with poly-D-lysine (Sigma, USA). After 1h cells were fed with fresh neurobasal medium (B-27 supplement / pen strep / L-glutamine) and maintained in a 5% CO<sub>2</sub> - 95% O<sub>2</sub> incubator at 37 °C.

### ***Immunofluorescence***

After 3 days of DRG neurons culture, the cells were fixed with 10% neutral buffered formalin solution for 20 min and permeabilized with PBS + 0.5% Triton X100 for 10 min. The cells were then incubated with blocking buffer (DPBS, 1% FBS) for 1 h prior to incubation overnight with primary antibody at 4 °C. The cells were then washed three times with DPBS and incubated with Alexa-Fluor conjugated secondary antibody for 1 h at room temperature. The cells were again washed three times with DPBS and incubated for 10 min with 5 µg/mL DAPI in DPBS. Finally, the cells were washed for the last time with DPBS. Confocal images were acquired with an automated confocal microscopy system (IN Cell Analyzer 6000, GE Healthcare Bio-Sciences AB, Uppsala, Sweden) using a 10× air lens (NA 0.45). Tuj-1 staining was detected using the 642 nm laser with a 706 nm emission filter, and DAPI staining was detected using the 405 nm laser with a 450 nm emission filter. Four fields per well were recorded.

#### ***DiSBAC2(3) Assay***

DRG neurons were stained for 2 h at 37 °C with pre-warmed plating medium containing 25 µM of DiSBAC2(3). The cells were then washed three times with the freshly-prepared sterile imaging buffer (150 mM of NaCl<sub>2</sub>, 5 mM of KCl, 10 mM of HEPES, 2 mM of CaCl<sub>2</sub>, 2 mM of MgCl<sub>2</sub>, 5.5 mM of glucose, and 2.9 mM of sucrose in distilled water, pH 7.5). After washing, the cells were incubated in 40 µL of imaging buffer for 30 min at 25 °C, to equilibrate the membrane potentials of sensory neurons. Prior to the inoculations of the compounds, a first set of images was acquired (Time 0) with the automated confocal microscopy system (IN Cell Analyzer 6000, GE Healthcare Bio-Sciences AB, Uppsala, Sweden). Riluzole, KCl, mycolactone, or DMSO as a negative control was then inoculated into the imaging buffer. After 30 min or 1 h of incubation at 25 °C, a

second set of images (Time 1) of the same location was acquired with the confocal microscopy system, using the same cells as those of “Time 0”, with the same settings. The images were acquired with an IN Cell Analyzer 6000 (GE Healthcare Bio-Sciences AB, Uppsala, Sweden), using a 20× air lens (NA 0.45), with an adjustable confocal aperture (1.07 AU). The focus height was adjusted to 3  $\mu\text{m}$ , and a  $2 \times 2$  binning was selected. DiSBAC2(3) staining was detected using the 561 nm laser with a 600 nm emission filter and a 0.35 ms excitation time for hyperpolarization or a 0.1 ms excitation time for depolarization. Between 4 to 16 fields per well were recorded.

### ***Image Analysis and Data Management***

Each image was processed using image analysis software (version 2.3.0, Perkin Elmer, Columbus, Waltham, MA, USA). As described in previous studies (Fenistein et al. 2008; Marion et al. 2014), two sets of images that were obtained using the same acquisition position, before and after the addition of neuroactive compounds or DMSO, were analyzed. Each pixel was assigned a threshold value according to DiSBAC2(3) intensities. The threshold of DiSBAC2(3) intensity from the glial cells area was defined as a background signal. The pixels with intensities lower than the background threshold were filtered to “0”. Otherwise, the pixels with intensities above the threshold were allowed to define regions of interest concerning DRG neurons. The DiSBAC2(3) intensities in the selected regions were measured using the analysis software (Columbus, Perkin Elmer). The membrane potential changes in the cells, under the effect of tested compounds, were determined for each well as the ratio (Equation (1)) of the sum values defining the intensities of the positive DiSBAC2(3) before and after the addition of neuroactive molecules or DMSO: Ratio = (sum intensity of

DiSBAC2(3) at Time 0)/(sum intensity of DiSBAC2(3) at Time 1) (1) Neurites were detected on the Tuj-1 positive neuronal cell images based on higher intensity values, compared to the surroundings. The first step of an image's analysis consisted in the segmentation of nuclei in Tuj-1 positive cell populations. Next, the neurite algorithm (CSIRO Neurite Analysis 2 method in the Columbus image analysis software) was used to detect neurites and neurite trees. For each individual cell, the Maximum Neurite Length as well as the length of the longest neurite attached to the Tuj-1 positive nucleus was recorded.

### ***Cytotoxicity Assay***

Mycolactone was added at various concentrations to a 384-well microtiter plate containing the cultivated DRG neurons. After incubation with mycolactone for 24 h, cell toxicity was quantified using the Toxilight bioassay sample kit (Lonza, Walkersville, MD, USA). ToxiLight™ 100% lysis reagent was added as a positive control, allowing for the assessment of the full toxicity. The percentage of viability was normalized (100% viability with vehicle (0  $\mu$ M mycolactone) and 0% viability with the lysis reagent). Mycolactone in DMSO was diluted 500-fold in complete cell medium prior to the assay.

### **Competition Binding Experiment**

HEK293 cells transfected with 20 ng of SNAP-AT2R plasmids were seeded at a density of 50,000 cells per well in 96-well white plates. Twenty-four hours (24 h) after transfection, SNAP-AT2R was labeled for 1 h at 37 °C with 100 nM BG-Lumi4-Tb diluted in Tag-lite labeling buffer and washed four times. The fluorescent ligands and compounds to be tested were diluted in Tag-lite labeling buffer. A saturation binding experiment was performed on HEK293 cells

overexpressing SNAP tagged AT2R using increasing concentrations of fluorescent DY647-AngII ligand. Competition binding experiments were performed using natural ligand fluorescently labelled AngII (DY647-AngII). A fixed concentration of fluorescent angiotensin-II ligand was used as determined by saturation binding experiments ( $3 \text{ nM} = K_d$ ) in the presence of increasing concentrations of the compounds to be tested (mycolactone, EMA401, and C21). In the plate containing the labeled cells,  $50 \mu\text{L}$  of the compounds to be tested were added prior to the addition of  $50 \mu\text{L}$  of fluorescent angiotensin-II. The plates were incubated for 3 h in the dark at  $4^\circ\text{C}$  before signal detection. HTRF signal detection was performed on a PHERAstar (BMG Labtech, Champigny-sur-Marne, France). The signal was collected both at 665 nm and 620 nm. The HTRF ratio was obtained by dividing the acceptor signal at 665 nm by the donor signal at 620 nm and multiplying this value by 1000. The data points were obtained in triplicates, and fitting was performed using GraphPad Prism (version 5.03, GraphPad Software, Inc., San Diego, CA, USA). The  $K_d$  and  $K_i$  values are represented as average values for three independent experiments.

### ***Electrophysiology***

Whole-cell patch-clamp was performed using an EPC-10USB amplifier (HEKA, Lambrecht, Germany) and the PATCHMASTER software (HEKA, version 2  $\times$  90.1). The resistances of the patch electrodes were 2–5  $\text{M}\Omega$ . Cells harvested on a 12 mm coverslip were current-clamped close to their resting potential ( $-55$  to  $-65 \text{ mV}$  in average). The pipette solution was composed of K-gluconate 145 mM,  $\text{MgCl}_2$  2 mM,  $\text{CaCl}_2$  1 mM, EGTA 10 mM, HEPES 5 mM, and K2ATP 5 mM, adjusted to pH 7.2–7.3 with KOH; osmolarity was 300 mOsm. The extracellular solution for the current-clamp experiments contained  $\text{NaCl}$  140 mM, KCl 5 mM,

MgCl<sub>2</sub> 1 mM, CaCl<sub>2</sub> 2 mM, HEPES 10 mM, and glucose 10 mM, adjusted to pH 7.4 with NaOH; osmolarity was 310 mOsm. The membrane potential was continuously monitored for 20–25 mins after Riluzole or KCl application.

### *Statistics*

Statistical significance (p-value) was evaluated with a two-tailed unpaired t-test, Mann–Whitney test or ANOVA using Dunnett's Test (GraphPad Software, Inc., San Diego, CA, USA).

# RESULTS

## **Analgesic effect of mycolactone *in vivo* pain models**

To examine the analgesic property of mycolactone, I first used formalin-induced acute inflammatory pain model. The Injection of 1% formalin with 5 $\mu$ M mycolactone (i.pl) induced significantly less inflammation, shown as paw thickness, 2 hours after injection compared to 1% formalin and vehicle injected group (**Fig. 6 A, 6B**). Also, a significant decrease of noxious behavior (licking and flinching of the paw) in the second phase of formalin test was found in 1% formalin with 5 $\mu$ M mycolactone group (**Fig. 6C, 6D**). Moreover, to test the analgesic effect of mycolactone in neuropathic pain condition, I used the CCI model. As mycolactone easily diffuses through spinal meninges, I injected 0.5 and 5 $\mu$ M of mycolactone intrathecally to deliver mycolactone directly to DRG 14 days after surgery. By measuring the changes of threshold in response to mechanical stimulations with a series of von Frey filament, mycolactone increased the mechanical threshold in 5 $\mu$ M injection but not in 0.5 $\mu$ M, thus inducing analgesia in neuropathic mice in a dose dependent manner (**Fig. 6 E**). The effective dose of mycolactone (5 $\mu$ M) also showed an analgesic effect towards thermal hyperalgesia as tested with the Hargreaves test (**Fig. 6 F, 6G**).

## **Development of a Medium-Throughput Visual Assay of DRG Neurons**

To assess the ability of mycolactone to induce the hyperpolarization of nociceptive DRG neurons, I developed a dedicated, streamlined, automated assay. More precisely, I established and optimized a DiSBAC2(3) image-based automated confocal microscopy assay, relying on the monitoring of membrane potentials. The development focused mainly on the miniaturization of the

automated assay, enhancing the quality of data, and reducing the number of mice (see Materials and Methods) needed per experiment. To achieve this challenge, I optimized the conditions of miniaturization for dissociated DRG neuron cultures in 384-well micro-titer plates. More specifically, for the optimizations, several parameters were monitored, including those relevant to the methods of dissociation, the density of DRG neurons per well, the enrichment in DRG population, and the presence of neurites. Indeed, the cell density parameter is essential for the image acquisition protocol with the automated microscope as well as for ensuring proper neuronal connectivity. The optimization process thus led me to set the number of seeded cells per well to 4000, which consisted in a mixed population of DRG neurons and non-neuronal cells. After three days of selection using Ara-c and FdU to impede the survival of non-neuronal cells, images were acquired on the confocal microscope with a 20× magnification, leading to the detection of about 20 to 30 small- and medium-sized DRG neurons per image. In order to determine the exact number of DRG neurons in a microplate at this time point, the cells were stained for  $\beta$ -III tubulin using Tuj-1 antibody, and I found that, on average, 65% of detected cells were Tuj-1 positive (**Fig. 7A, 7B**). Thus, this system typically allows for the analysis of more than 100 different conditions with a very small number of mice (typically 4–6). In parallel, the health of cultured DRG neurons was assessed by monitoring neurite development. As shown in **Figure 7C**, the neurite growth of the DRG neurons was assessed by bright-field time-course imaging, after 48 h and 72 h of culture, with neural connectivity estimated based on cell density.

### **Monitoring Membrane Potentials of DRG Neurons with DiSBAC2(3)**

I adapted the procedures relying on the use of DiSBAC2(3) as a



fluorescent indicator to monitor the membrane potentials of DRG neurons with the miniaturized visual automated assay. In the previous studies concerning macrophages and hippocampal neurons (Marion et al. 2014), they have suggested the use of DiSBAC2(3) at 150  $\mu$ M concentration. However, in the present case, image analysis becomes difficult and cumbersome at such a concentration, as the DRG neurons are saturated by DiSBAC2(3). In addition, in such conditions the non-neuronal cells were also stained by DiSBAC2(3) (data not shown). To alleviate these difficulties, I tested different concentrations of DiSBAC2(3). The tests allowed us to determine the appropriate concentration of DiSBAC2(3) (25  $\mu$ M) to ensure a proper image analysis of DRG neurons (**Fig. 8A**). Indeed, at such concentration, the fluorescence intensity level of non-neuronal cells appears to be low (because of the differences in the native resting membrane potentials for the various cell types), making possible its elimination as a background level using image analysis software. In addition, it was possible to ascertain the stability of DiSBAC2(3) staining intensity over an hour period (**Fig. 8B**). This stability renders the system suitable for the study of compounds with long-lasting effects on DRG membrane potentials, with the reproducible assays displaying high sensitivity to small variations of membrane potentials. More specifically, I showed that miniaturized assay allows for the visualization of membrane potential changes by treating DRG neuron cultures with KCl (depolarizing agent) (Willenborg et al. 2012) or with Riluzole (hyperpolarizing agent) (Cadaveira-Mosquera et al. 2011; Xing et al. 2003). The dose-response curves of the compounds with Riluzole and KCl in DiSBAC2(3) assays on DRG neurons (**Fig. 9A, 9B**) showed that (1) Riluzole triggers a decrease in cell fluorescence below 25  $\mu$ M, indicative of cell hyperpolarization, and (2) KCl triggers an increase in cell fluorescence above 30 mM, indicative of cell depolarization. Maximal

effects were observed at 100  $\mu$ M Riluzole and at 50 mM KCl (**Fig. 9C, 9D**). It is worth noting that a major strength of my assay, with the imaging time of 0.07 ms per field, resides in the possibility to compare diverse conditions on the same plate. For further validation of my image analysis process, the assays were paralleled by patch-clamp experiments (**Fig. 9E**). The results showed that slow acting drugs such as Riluzole induced the gradual hyperpolarization of membranes for approximately 8 min after the compound's addition, with the effect plateauing after that time. On the other hand, the high concentration of KCl induced the rapid depolarization of membranes, with the effect plateauing 1 min after the KCl's application. In **Figure 9**, the fluorescence data are plotted on the corresponding values for membrane potentials, as described by a previous study (Sguilla et al. 2003). Briefly, the maximal effect of Riluzole is associated with a decrease of about 44% in cell fluorescence, corresponding to a variation of 15 mV as recorded by patch-clamp. On the other hand, KCl provokes an increase of about 32% in cell fluorescence, corresponding to a variation of 55 mV as recorded by patch-clamp (**Fig. 9D, 9E**). The data are in accordance with other studies using DiSBAC2(3) to visualize membrane potential changes.

### **Mycolactone Induces Hyperpolarization of DRG Neurons at Non-Cytotoxic Doses**

In the previous study concerning macrophages, PC12 cells, and hippocampal neurons, they showed that mycolactone, at non-cytotoxic doses, induces membrane hyperpolarization (Marion et al. 2014). More specifically, mycolactone induced cell hyperpolarization by targeting angiotensin pathways, and binding to AT2R. Based on these results, I hypothesized that hyperpolarization induced by mycolactone binding to AT2R could cause local

analgesia, and I confirmed this hypothesis in animal models. With the methodological development above, we can extend the study of the effect of mycolactone to DRG neurons involved in pain signals. For DRG neurons, we first evaluated the cytotoxic effect of mycolactone, for concentrations ranging between 0.4  $\mu$ M and 70  $\mu$ M, over a three-day period using the Toxilight bioassay kit. For the tested concentration range, no significant cytotoxic effect was observed at 24 h post-addition of mycolactone (**Fig. 10A**). At 48 h, 80% of the DRG neurons were still viable up to the maximal tested concentration of 70  $\mu$ M (**Fig. 10B**). At 72 h, the vehicle (DMSO 0.2%) started to exhibit toxicity, with about 80% of viable cells, whereas about 60% of DRG neurons remained viable for the mycolactone samples at all of the tested concentrations (**Fig. 10C**). DRG neurons cultured in 384-well plate did not survive to 96-hour incubation after 3-day seeding. As a matter of fact, under such conditions, most of the DRG neurons had died in the vehicle control (less than 20% viability), making it impossible to assess the cytotoxic effects of mycolactone at this time point. Altogether, my data showed that DRG neurons are far less sensitive to the cytotoxic effects of mycolactone compared to other cell types (**Table 1**). Similar conclusions were reached for hippocampal neurons (Marion et al. 2014). On the other hand, with the exception of T lymphocytes, HEK293T, and Huh7, mycolactone appears to kill many different types of cells at such concentration (**Table 1**). Next, I showed in Figure 5A that mycolactone was able to hyperpolarize DRG neurons at concentrations above 1  $\mu$ M. The level of hyperpolarization induced by mycolactone is dose-dependent. No effect could be observed at submicromolar concentrations. The maximal effect was recorded at 30 min post-addition of mycolactone and remained maximal during one hour. In all subsequent experiments, the dose of mycolactone was set at 3.5  $\mu$ M, checked to be non-

cytotoxic even after 24 h of exposure (**Fig. 10A**), with the hyperpolarization effect further validated by patch-clamp experiments (**Fig. 11B, 11C**). In addition, monitoring the neurite growth showed that exposure to mycolactone at a concentration of 3.5  $\mu$ M for 60 min did not affect neurite lengths (**Fig. 11D**). Furthermore, expectedly, mycolactone did not induce hyperpolarization in DRG neurons isolated from AT2R-knock-out mice (**Fig. 11E**). Altogether, the data show that mycolactone induces hyperpolarization in DRG neurons targeting specifically angiotensin II type 2 (AT2) receptors. I then wanted to further characterize in DRG neurons the specific interaction between mycolactone and AT2R, leading to cell hyperpolarization. To pinpoint the specificities of mycolactone/AT2R interactions, I tested in my assay known ligands of AT2R: (i) angiotensin II; (ii) EMA 401, known to alleviate neuropathic pain through AT2R; and (iii) C21 endowed with anti-inflammatory capabilities, targeting AT2R (**Table 2**) (Anand et al. 2013; Anand et al. 2016; Wan et al. 2004). As shown in **Figure 12**, all of these compounds are not able to trigger the hyperpolarization of DRG neurons, in contrast to mycolactone. Moreover, the co-incubation of EMA 401 and C21 with mycolactone did not affect the hyperpolarization mediated by mycolactone. Altogether, these results further demonstrate that the mycolactone-mediated signaling that triggers hyperpolarization is not inhibited by these AT2R ligands.

Figure 6

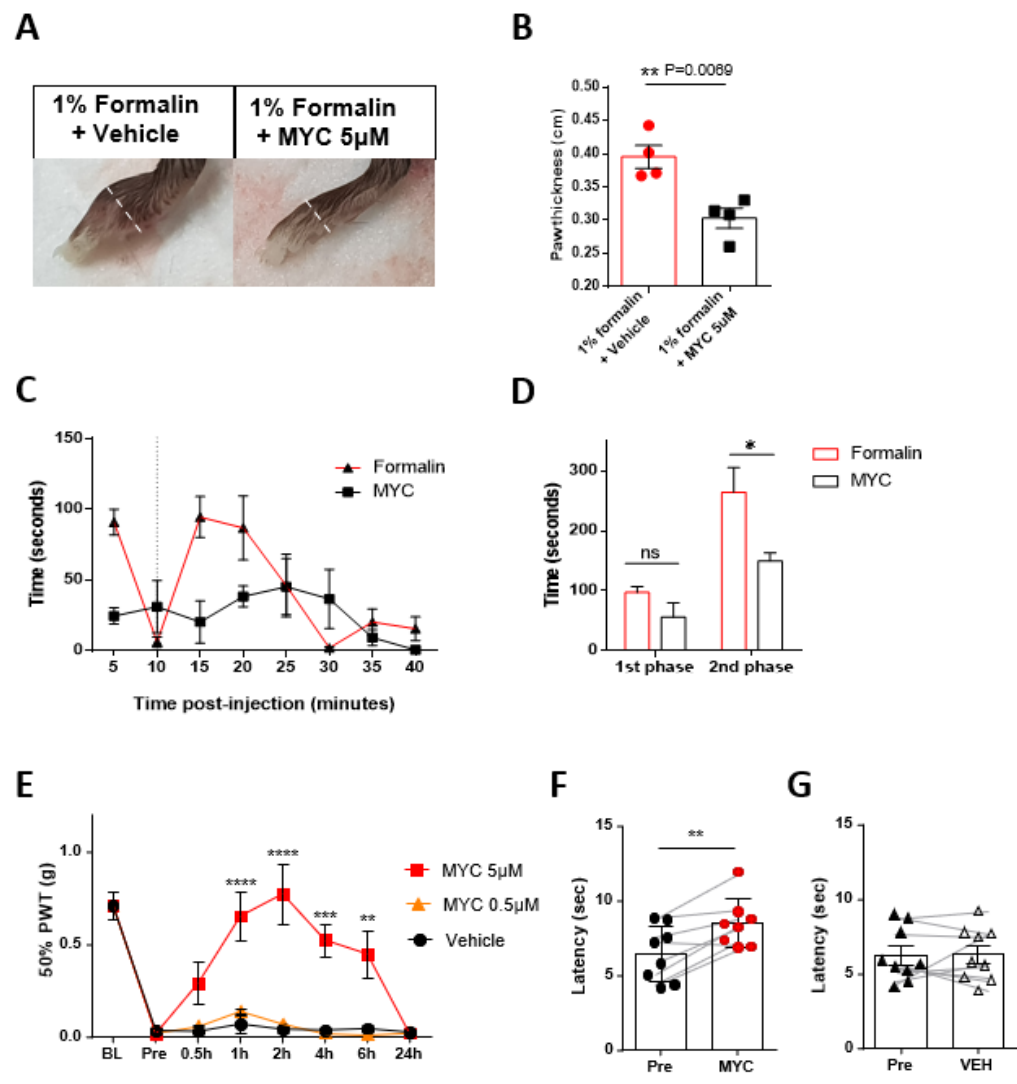


## **Figure 6. Mycolactone induced analgesia in various pain models.**

(A) Mouse hind paw 2 hours after 1% formalin injection with vehicle or 5 $\mu$ M Mycolactone (MYC). (B) The bar graph representing the paw thickness of the mice 2 hours after formalin injection. (C) Effects of mycolactone on the time course curves of formalin-induced pain behavior. (D) Formalin-induced pain behavior was divided into two phases and analyzed. The bar graph represented the first phase (0–10 min) and second phase (10–40 min) of formalin-induced pain behavior. (D) Ipsilateral mechanical withdrawal threshold measured and compared before the injection with 30 min, 1, 2, 4, 6, 24 hours post intrathecal (i.t.) injection of mycolactone (MYC, 0.5 and 5 $\mu$ M) to the vehicle in von Frey test.  $**P < 0.001$ ,  $****P < 0.0001$ , Two-way RM ANOVA followed by post hoc Bonferroni's test. Error bars represent SEM. (n=8, each group). Hargreaves test after i.t. injection of (E) Mycolactone 5 $\mu$ M and (F) Vehicle  $*p < 0.05$ ,  $**p < 0.01$  and  $***p < 0.001$  (Paired t test).

Figure 7.

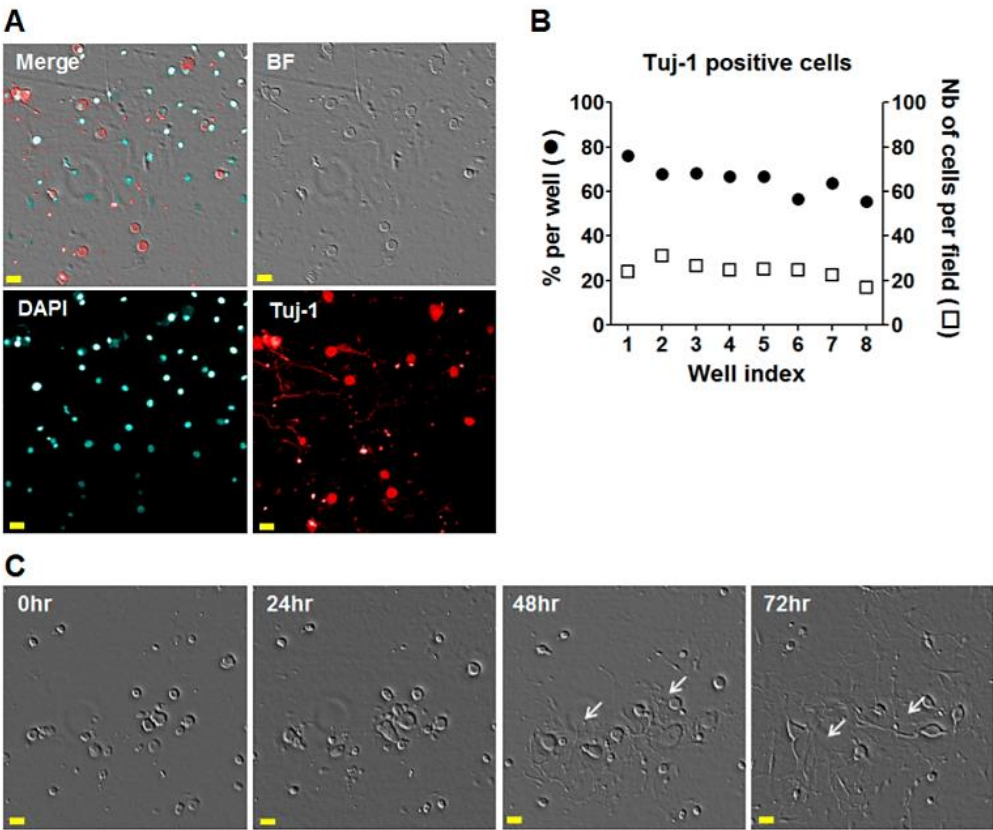


**Figure 7. Morphology of the Dorsal Root Ganglion (DRG) neurons 3 days after harvesting in 384-well microplates.**

(A) Bright-Field (BF) and confocal images. DRG neurons were labelled for Tuj-1 monoclonal antibody, allowing the detection of neuron-specific beta-tubulin III. DAPI-staining was used for nucleus labelling. Scale bar = 20  $\mu$ m; (B) Percentage of Tuj-1 positive cells per well and number of Tuj-1 positive cells per field. The percentage of Tuj-1 positive cells was determined for 200 cells in average; (C) BF images of DRG neurons at 0, 24, 48, and 72 h after plating in microplate; Scale bar = 20  $\mu$ m; White arrow, neurite growth.



Figure 8.

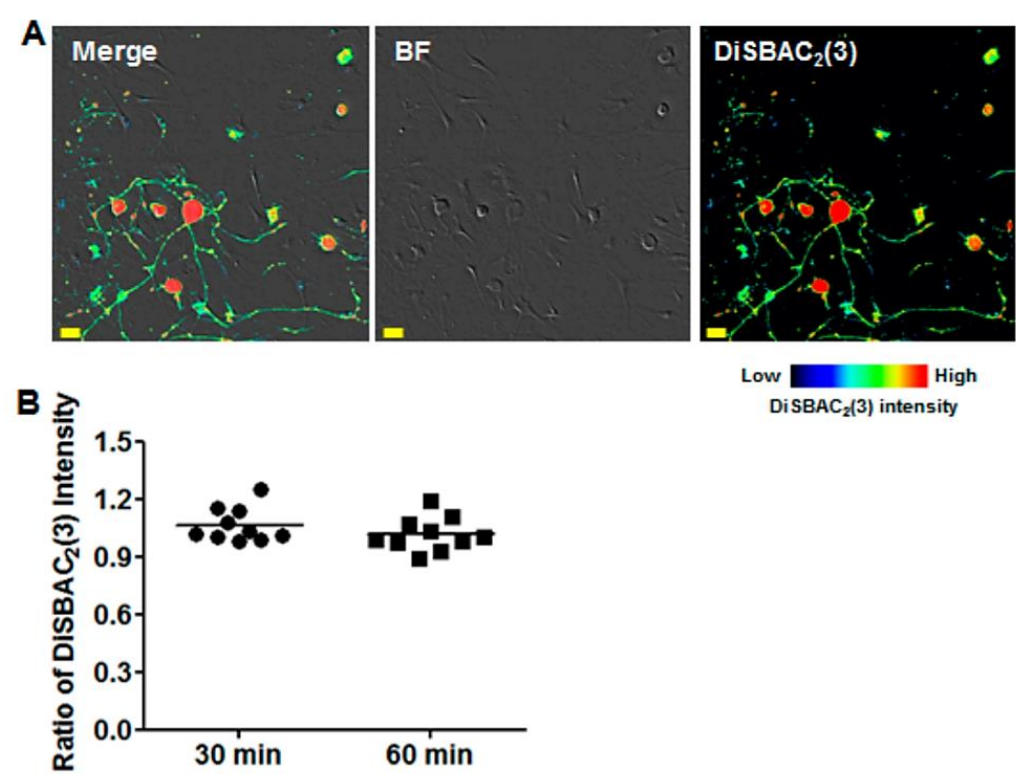


**Figure 8. Stability of DiSBAC2 (3) intensity in DRG neurons.**

(A) Bright-Field (BF) and confocal image of DRG neurons loaded with 25  $\mu$ M DiSBAC2 (3); Scale bar = 20  $\mu$ m; (B) Quantification of DiSBAC2 (3) intensities presented as ratios: the signal intensities were calculated by normalizing the DiSBAC2 (3) intensity at 30 min and 60 min to that before addition; each point corresponds to the mean value over 10 wells (corresponding to at least 1200 cells).

Figure 9.

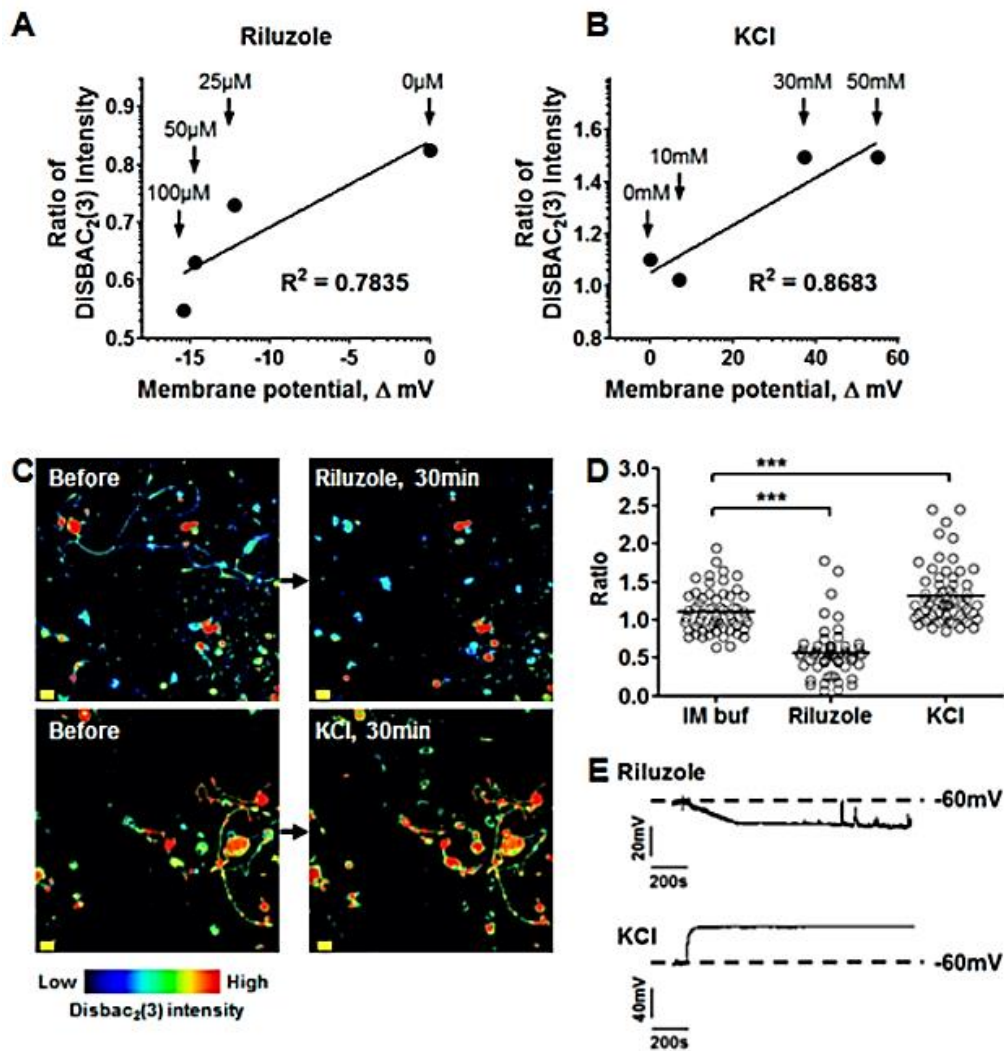


### **Figure 9. Change in membrane potential in DRG neurons.**

(A,B) Membrane potential measured by patch-clamp experiments (X-axis, n = 5 cells) and DiSBAC2 (3) assays (Y-axis, n >180 cells) for Riluzole (A) at concentrations of 0, 25, 50, and 100  $\mu$ M and for KCl (B) at concentrations of 0, 10, 30, and 50 mM. The  $\Delta mV$  and the ratio of DiSBAC2 (3) were calculated by normalizing the fluorescence intensity at 20 min to that at 0 min; (C) Images of DRG neurons before and after addition of Riluzole (100  $\mu$ M) or KCl (50 mM); Scale bar = 20  $\mu$ m; (D) Change in membrane potential after addition of Riluzole (100  $\mu$ M) or KCl (50 mM). The ratio was calculated by normalizing the intensity at 20 min to that at 0 min; \*\*\* p-value < 0.0001; (E) Representative chart recording traces of the membrane potential of DRG neurons treated with Riluzole (100  $\mu$ M) or KCl (50 mM).

**Figure 10.**

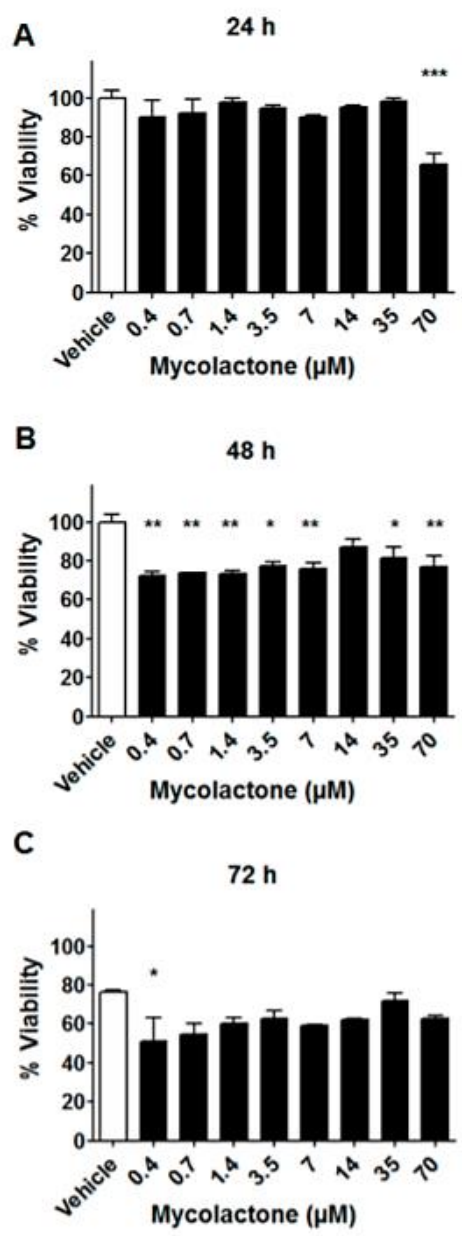


**Figure 10. Time dependence of the effect of mycolactone on the viability of DRG neurons.**

Viability of DRG neurons after different incubation times with mycolactone: (A) 24 h, (B) 48 h, and (C) 72 h. Each bar corresponds to the mean value of two wells (that have been harvested with 600 cells). p-values were calculated by ANOVA using Dunnett's Test for multiple comparisons to the vehicle control, \*\*\*  $p$ -value  $< 0.001$ ; \*\*  $p$ -value  $< 0.01$ ; \*  $p$ -value  $< 0.05$ .

Figure 11.

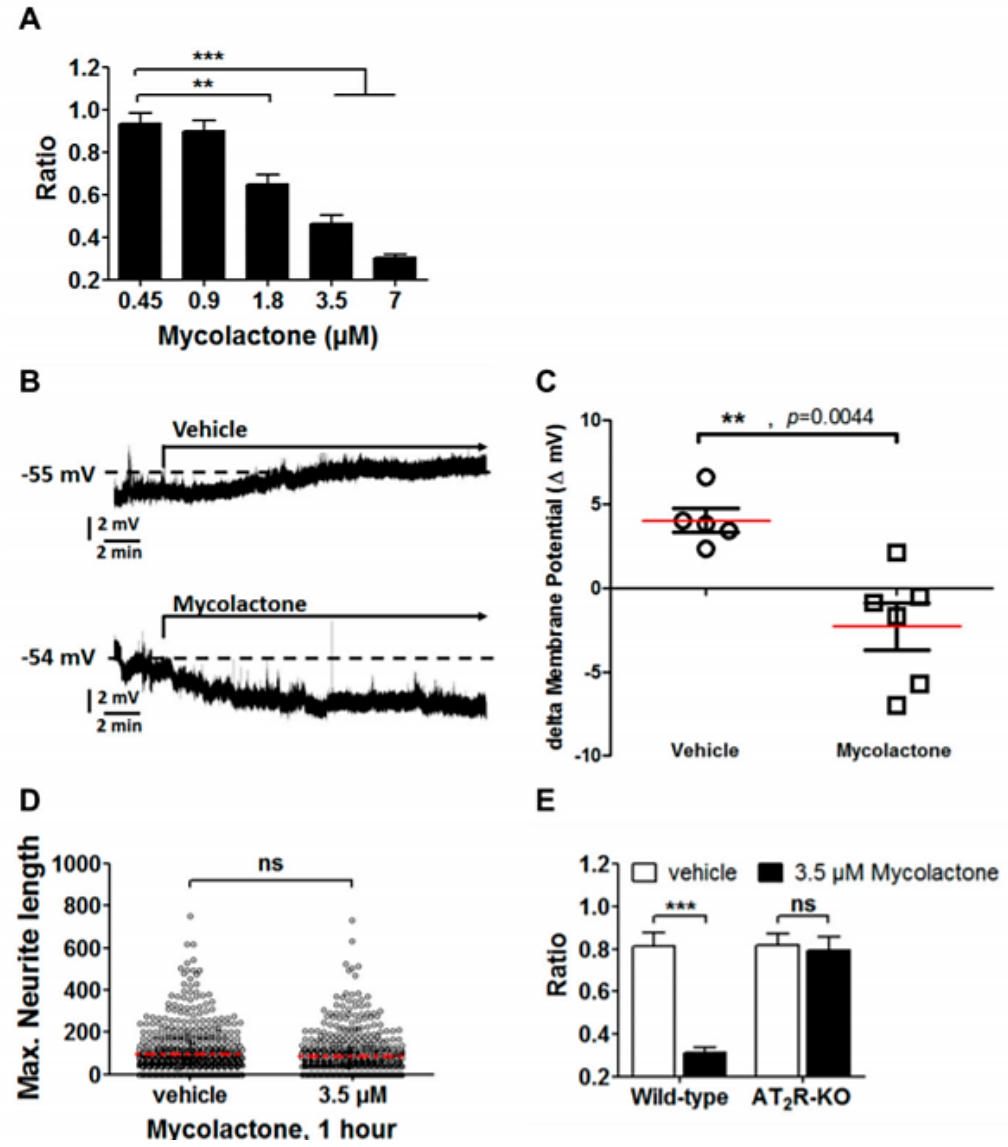


## **Figure 11. Characterization of the effects of mycolactone on DRG neurons.**

(A) Hyperpolarization of DRG neurons upon addition of mycolactone at different concentrations. The ratio corresponds to the intensity of the DiSBAC2 (3) dye before addition and after one hour from the addition of mycolactone. A ratio lower than 0.6 corresponds to hyperpolarization; (B,C) Membrane potential recording by patch-clamp. Representative chart recordings of the membrane potential of DRG neurons challenged either by 0.2% DMSO (vehicle) or mycolactone (3.5  $\mu$ M) (B). Pooled data illustrating hyperpolarization triggered by continuous application of mycolactone for 20 min. Red line: mean (C); (D) Maximum neurite length in Tuj-1 positive neurons incubated with (n = 499) or without (n = 583) mycolactone; Mann–Whitney test; ns, not significant; Red dot line, mean; (E) Quantification of the DiSBAC2 (3) ratio for DRG neurons from wild-type and AT2R deficient (AT2R-knock-out (KO)) mice after loading with 3.5  $\mu$ M mycolactone for 1 h; \*\*\*  $p$ -value < 0.0001; \*\*  $p$ -value < 0.001; ns, not significant.



**Figure 12**

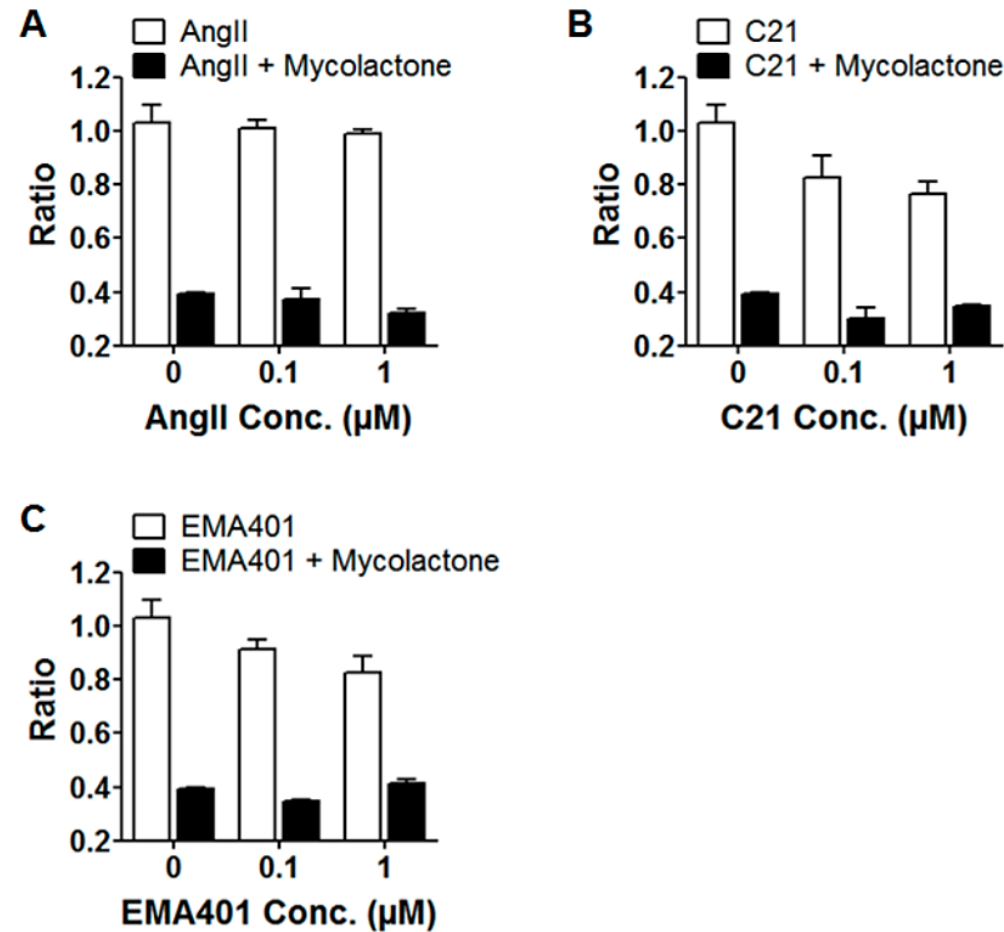


**Figure 12. Effect of high affinity ligands to AT2R on DRG neurons.**

(A–C) DiSBAC2(3) fluorescence of DRG neurons calculated as the ratio before and after treatment with ligands for 30 min (white bar). After 30 min incubation with the compound, mycolactone at 3.5  $\mu$ M was added for 30 min (black bar); (A) Angiotensin II, (B) C21, or (C) EMA401; minimum two wells per condition were analyzed (including at least 200 cells).

Figure 13

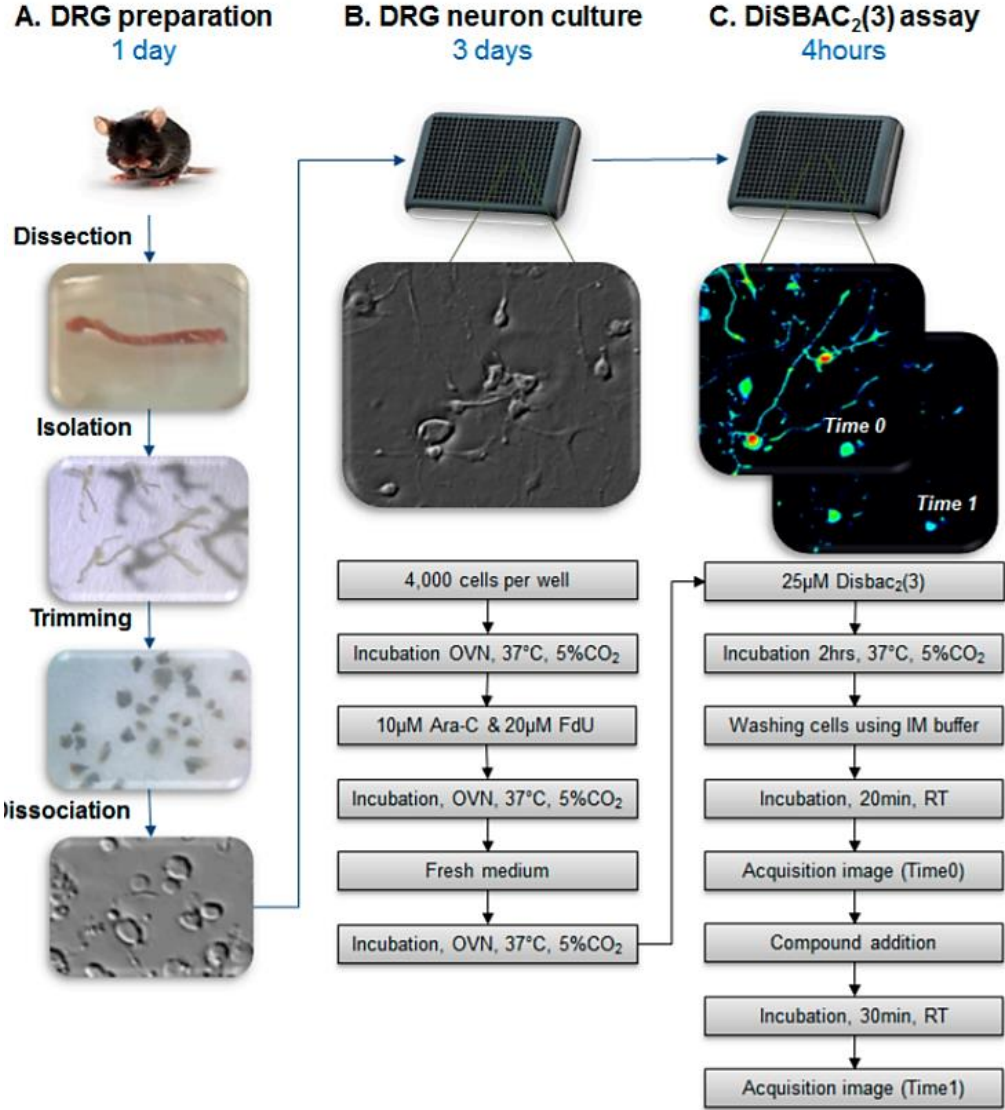


**Figure 13. Schematic overview of dorsal root ganglion (DRG) culture and DiSBAC2 (3) assay in a micro-titer plate.**

(A) DRG preparation; (B) DRG neuron plating and culture during three days; (C) DiSBAC2 (3) assay in the micro-titer plate.

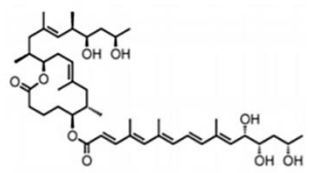
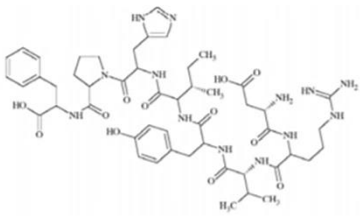
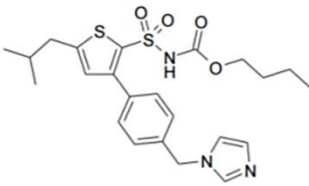
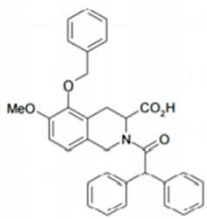
**Table 1**

Cytotoxicity induced by mycolactone in different cell types.

Cell Type	Cytotoxicity by Mycolactone A/B		
	Concentration	Incubation Time	% of Cytotoxicity
Peripheral blood lymphocyte	1 µg/mL	90 h	40%
Mouse fibroblast (L929)	15 µg	4 h	>80%
Mouse fibroblast (L929)	60 ng/mL	48 h	75%
Mouse fibroblast (L929)	15 ng/mL	48 h	100%
Peripheral blood human neutrophils	5.3 µg	4 h	>80%
	1 µg	24 h	100%
Keratinocyte stem cell (TAC)	100 ng/mL	24 h	>80%
human keratinocyte line (HaCaT)	1 µg/mL	24 h	>30%
Human hepatoma (Huh7)	1 µg/mL	24 h	0%
Embryonic kidney (HEK293T)	1 µg/mL	24 h	0%
Human primary adult skin keratinocytes	>30 ng/mL	72 h	80%
Endothelial cells (HUVEC)	7.8 ng/mL	4 days	80%
Hippocampal neurons	40 µg/mL	24 h	40%
Mouse bone marrow-derived dendritic cells	100 ng/mL	48 h	50%

# Table 2

Ligand binding affinities to AT<sub>2</sub>R.

Ligand	Chemical Structure	K <sub>i</sub> to AT <sub>2</sub> R
Mycolactone		20 μM
AngII		0.1 nM
C21		1 nM
EMA401		4 nM

## DISCUSSION

*Mycobacterium ulcerans* is the causative agent of Buruli ulcer, a neglected and emerging infectious disease (Adusumilli et al. 2005; Organization 2012). This infection often provokes several massive cutaneous ulcers (O'Brien et al. 2014). A singularity of the lesions resides in the lack of pain, with, as a consequence, patients not seeking appropriate medical care. In Buruli ulcer, the lesions are caused by mycolactone, the main known virulence factor of *M. ulcerans*. Mycolactone has been associated with various effects such as the induction of cell death or immunomodulatory effects (Sarfo et al. 2016). Mycolactone was shown to act on different types of cellular receptors and signaling pathways (Bieri et al. 2017). It has first been shown by Guenin-Macé and colleagues that mycolactone induces skin lesions by hijacking the Wiskott–Aldrich syndrome protein (Guenin-Macé et al. 2013). Concomitantly, Hall and colleagues reported that mycolactone-induced cytotoxicity was caused by the inhibition of Sec61-dependent translocation, leading to profound changes in cellular signaling (Hall et al. 2014). These findings were further substantiated by a report by Baron et al. demonstrating that Sec61 is the host receptor for the mycolactone-mediated immunomodulation, leading to the current understanding that Sec61 is the major target underlying the cytotoxicity of mycolactone (Baron et al. 2016). Furthermore, mycolactone was shown to promote Bim-dependent apoptosis via the mTor pathway (Bieri et al. 2017). It is thus very likely that, as a multi-target weapon, mycolactone triggers several signaling pathways leading to massive skin destruction but also to analgesic effects. In this background, I have first demonstrated the mycolactone induced analgesia in various pain models such as acute inflammatory pain model and neuropathic pain model (**Fig.**

6). I have thus attributed this effect to the capability of mycolactone to trigger a sustained hyperpolarization of neurons. Moreover, the detailed cellular pathway underlying this effect was identified, showing that hyperpolarization is triggered upon the binding of mycolactone to AT2 receptors, leading to the activation of TRAAK channels (Marion et al. 2014). Overall, their results suggested that the implementation of analgesia in Buruli ulcer could inspire the development of new efficient analgesics, based on the properties of mycolactone acting on the AT2R/TRAAK system. In such a context, it was then mandatory to extend the studies to DRG neurons, as the sensory neurons are involved in relaying of pain signals. Here, I characterized the effect of mycolactone on DRG neurons, acting on the AT2 receptor. I thus adapted the fluorescence based that was used to identify the signaling pathway involved in mycolactone mediated hyperpolarization to DRG neurons (Marion et al. 2014).

On methodological grounds, I developed an efficient medium-throughput high-content imaging assay (**Fig. 13**), which can represent a powerful alternative to electrophysiology. As such, this development can be valuable for its own sake in studies aiming to understand the physiology of DRG neurons and/or to identify active compounds modulating the membrane potentials. This work allowed for pinpointing the major advantages gained with the development of the imaging assay as compared to the patch-clamp technique. These advantages can be conveniently summarized following three main axes:

(1) Accessible scope: from low-throughput to medium-throughput

A major strength of the DiSBAC2(3)-based high-content imaging assay resides in the quantitative jump in the scope of analysis made possible, concerning the number of cells and the number of different conditions. Thus, with the patch-clamp technique the scope of analysis is typically limited to 15 cells



per experience (and per day). Such a limitation makes it difficult to implement a large number of control conditions. By comparison, the imaging assay permits a medium-throughput scope, with the possibility to implement typically 100 different conditions, with 400 cells per condition. It becomes then possible to envision the routine screening of small-size libraries, and performing dose-response tests, with the possibility of several replicates for each assay.

## (2) Accessible cell sizes

In the patch-clamp technique the size of cells accessible to the experiments is limited by the size of electrodes, thus impeding for example the analysis of neurites. By comparison, no such limit exists with the imaging assay, and notably it becomes perfectly feasible to analyze the membrane potentials of neurites.

## (3) Miniaturization and homogenization of experimental conditions

A notable advantage of the imaging assay is that it allows the miniaturization of the experimental conditions in terms of the volumes of the test solutions. Thus, the volumes required are typically in the range of 50  $\mu\text{L}$ , as compared to the bulk test solutions required for patch-clamp which are typically in the range of 500  $\mu\text{L}$  per reservoir for one cell. Such an advantage can be critical, notably when the tested compounds are available in small quantities. On the other hand, the experimental settings in the imaging assay allow for the obtaining of a high degree of homogeneity in the recording conditions, with typically 400 cells analyzed in the same conditions. By comparison, such homogeneity is not achieved with the patch-clamp technique, with the possibility for each cell to be analyzed in different environmental conditions such as for temperature.

In addition, beyond the various technical considerations above, it is worth highlighting the easiness of use of the imaging assay, as compared to the

skilled experience required for the patch-clamp technique. Nevertheless, of course for certain types of specific analyses, patch-clamp is the technique of choice, for example when high sensitivity (pA resolution) is required, or for noise measurements of currents passing through low-conductance (pS) channels. Concerning the effect of mycolactone on DRG neurons, I demonstrated that non-cytotoxic doses provoke hyperpolarization of the neurons, targeting AT2R. Interestingly, my results showed that the DRG neurons were less prone than other cell types to the cytotoxic effects of mycolactone. (**Table 1**). I show that AT2R is not involved in mycolactone-mediated cell death, as the viability of DRG neurons from AT2R-deficient mice is similar to that of wild-type mice upon mycolactone addition. It is worth mentioning that my results are in contrast with those reported by Anand et al. (Anand et al. 2016), notably concerning the cytotoxicity of mycolactone in DRG neurons. More precisely, in this study, the cytotoxicity result appears as part of a demonstration essentially aiming to invalidate the analgesic effect of mycolactone targeting specific pathways, favoring the model of nerve destruction similar to the leprae case. In this respect, Anand et al. report that mycolactone induces a loss of neurites in DRG neurons after incubation at 0.1  $\mu$ M for 24 h, whereas we do not observe such an effect in the settings up to 35  $\mu$ M (data not shown). Indeed, such effect on neurite outgrowth is typically used as a correlate of neuronal cytotoxicity. In addition, it was also reported in this study that, at 48 h, mycolactone-treated cultures displayed reduced Gap43 and  $\beta$ -tubulin expressions, as well as mitochondrial clumping, which further correspond to indications of cytotoxicity. At present, it is not possible to account straightforwardly for such discrepancies between the two studies, and only further experiments could help clarify the situation. It is nevertheless relevant to notice that the study by Anand and colleagues concerned

human and rat DRG neurons. Even though not very plausible, one possible explanation for the discrepancy between the two studies may come from different sensitivity to the cytotoxicity of DRG neurons, following species. Beyond this argument concerning cytotoxicity, it is interesting to notice that in their demonstration, Anand et al. invoke the absence of the effect of Angiotensin II or the AT2R antagonist EMA401 in their settings to hint that mycolactone could in effect not target the AT2R receptors. As a matter of fact, I fully account for this observation, as I demonstrated that, as a difference to other known ligands of AT2R (agonists or antagonists, including Angiotensin II, C21, and EMA 401) (Anand et al. 2013; Anand et al. 2016; Wan et al. 2004), only mycolactone appears able to trigger hyperpolarization of DRG neurons. Moreover, I demonstrated that EMA 401 or C21 do not inhibit hyperpolarization triggered by mycolactone. This observation pinpoints the specificity of mycolactone/AT2R interactions. On the other hand, interestingly, the cellular mechanisms reported to account for mycolactone-induced cell death involve hijacking different signaling pathways, such as the mTOR pathway or the pathway involving Sec61-dependent protein translocation into the ER (Baron et al. 2016; Bieri et al. 2017). This last signaling was shown to occur in cells which are susceptible to very low doses of mycolactone at 48 h in in vitro conditions (Bieri et al. 2017; Dangy et al. 2016). Such results then raise the possibility that mycolactone in DRG neurons could interfere with mTOR and Sec61 pathways. Concerning cell types, I compared the hyperpolarizing effect of mycolactone in various cell types (macrophages, pheochromocytoma cells (PC12), and hippocampal neurons). In PC12, a hyperpolarization of  $-10$  mV on average was found (Marion et al. 2014), while in DRG the hyperpolarization was of  $-7$  mV. However, using the fluorescence-based assay, essentially identical ratio values were obtained for

these two types of cells. These data suggest that there is no difference between the two types of cells concerning sizes of responses. In terms of doses of mycolactone, the PC12 cells appeared to be more sensitive than the DRG neurons. The explanation behind this difference requests further investigation.

Finally, in the perspective of the implementation of analgesia protocols, two important issues relative to practical conditions (concentrations) as well as fundamental mechanisms (AT2R signaling) will need to be considered in detail. Concerning the concentrations issue, it was reported by Sarfo and colleagues that the concentrations of mycolactone detected in lesions of BU patients are in the mid nM range (Sarfo et al. 2011; Sarfo et al. 2014). Such concentration is about one hundred-fold lower than what is required to trigger hyperpolarization in DRG neurons in vitro. However, the apparent high dose of mycolactone required to induce hyperpolarization may be overestimated due to experimental biases such as the strong affinity of mycolactone to plastic wares (including tips and microplate), thus limiting the effective amount of mycolactone available for the cell assay. There is also likely an issue with the stability of mycolactone in cell culture media, as well as upon light exposure (Marion et al. 2012). On the other hand, in tissues, upon infection, mycolactone is released by the bacilli within vesicles (Marsollier et al. 2007), with the possibility for concentration gradients occurring in the lesions. Noticeably, so far, mycolactone quantification relies on the total lipid extraction of skin biopsies or on whole blood quantification (Sarfo et al. 2011; Sarfo et al. 2014), and, accordingly, the local concentrations of mycolactone at the DRG neurons' contacts may be underestimated. Concerning the fundamental mechanisms, there is at present a lack of knowledge on the signaling of AT2R, and no functional assays are available to monitor AT2R activation in HEK cell models, for instance. The specificities of the receptor

(such as the absence of G-coupling or internalization) have been recently brought under new light with the elucidation of AT2R's crystal structure (Zhang et al. 2017). In this context, it does not appear possible to rank the activity of AT2R ligands based on their binding affinity and as stated in a recent review, the molecular mechanisms by which AT2R blockers mediate analgesia remain to be fully elucidated (Yekkiralala et al. 2017). The perspectives opened by the study for the development of new analgesics will then be embedded in the endeavors to characterize in detail the pharmacology and specificities of AT2R receptors and pathways.

## **CHAPTER 2:**

### **A $\beta$ accumulation in Vmo contributes to masticatory dysfunction in 5XFAD mice**

*\*THIS CHAPTER HAS BEEN LARGELY REPRODUCED FROM AN ARTICLE  
SUBMITTED TO JOURNAL OF DENTAL RESEARCH BY HAN-BYUL KIM\*,  
DOYUN KIM\*, HAYUN KIM, WHEEDONG KIM, SENA CHUNG, SEUNG-HYUN  
LEE, HYUNG RYONG KIM<sup>‡</sup> AND SEOG BAE OH<sup>‡</sup>*

## ABSTRACT

Alzheimer's disease (AD) shows various symptoms that reflect cognitive impairment and loss of neural circuit integrity. Sensory dysfunctions such as olfactory and ocular pathology are also observed and used as indicators for early detection of AD. Although mastication is suggested to correlate with AD progression, changes in the masticatory system have yet to be established in transgenic animal models of AD. In the present study, we have assessed pathological hallmarks of AD with the masticatory behavior of 5XFAD mice. We found that the masticatory efficiency and the maximum biting force were decreased in 5XFAD mice with no significant change in general motor function. Immunohistochemical analysis revealed significant accumulation of amyloid- $\beta$  ( $A\beta$ ), increased microglia number, and cell death in the trigeminal motor nucleus (Vmo) compared to other cranial motor nuclei that innervate the orofacial region. Masseter muscle weight and muscle fiber size were also decreased in 5XFAD mice. Taken together, the results demonstrate that  $A\beta$  accumulation in Vmo contributes to the masticatory dysfunction in 5XFAD mice, suggesting a close association between masticatory dysfunction and dementia.

# INTRODUCTION

Alzheimer's disease (AD) is one of the most common causes of dementia that results from the progressive degeneration of the central nervous system (Rosen et al. 1984). AD is generally thought to result from neuronal death caused by the accumulation of amyloid  $\beta$  ( $A\beta$ ) protein.  $A\beta$ , the neurotoxic peptide which is cleaved from amyloid precursor protein (APP), can further aggregate to form  $A\beta$  plaques that are commonly found in the brain of AD patients (He et al. 2018). Brain imaging of AD patients has revealed degeneration of symptom related brain regions such as hippocampus and this may cause memory deterioration (Deweert et al. 1995).  $A\beta$  accumulations are also seen in the temporal lobe, which may correlate to sensory and motor dysfunctions such as olfactory, ocular, and gait problems seen in AD patients (Frost et al. 2010; He et al. 2018; Lewis et al. 2006; Meshulam et al. 1998; O'Keeffe et al. 1996). However,  $A\beta$  accumulation has yet to be addressed in the orofacial sensorimotor system despite the correlation observed in oral dysfunction and cognitive impairment (Campos et al. 2017; Onozuka et al. 2000).

Recent clinical studies have found a significant cognitive decline in AD patients with oral impairments and masticatory malfunctions such as oral dyskinesia, periodontitis, and tooth loss (Campos et al. 2017; Singhrao et al. 2014). However,  $A\beta$  accumulation or neuronal loss in the mastication-related brainstem regions have yet to be observed in AD patients (Parvizi et al. 2001; Uematsu et al. 2018). APP and calpain-I are highly expressed and extensively colocalized specifically in the trigeminal motor neurons (Vmo) compared to the other cranial motor nuclei and are observed in brain regions with  $A\beta$  deposition in AD patients (Siman et al. 1990). This report suggests a correlation between  $A\beta$



accumulation in Vmo and masticatory dysfunction.

Transgenic AD mouse models were created to replicate the degenerative brain progression of human AD through the genetic mutation of APP and/or presenilin (PS) to increase A $\beta$ 40/42 production (Oakley et al. 2006). Of many transgenic AD models, 5XFAD (Tg6799) mouse is well known to cause A $\beta$  pathology as early as 1-2 months of age and impairment of spatial working memory by 6 months (Devi and Ohno 2010; Eimer and Vassar 2013; Lewis et al. 2006). In this study, we investigated whether Vmo manifests A $\beta$  pathology in 5XFAD mice and, if so, A $\beta$  pathology of Vmo is associated with masticatory dysfunction in an early stage (5 months old) of dementia.

# MATERIALS AND METHODS

## *Mice*

All experiments were performed with 5-months-old male 5XFAD (Tg6799; Jackson Laboratory, Stock #006554) and littermate mice. 4-5 mice were housed per cage at a temperature-controlled room ( $23 \pm 1^{\circ}\text{C}$ , 12/12 h light/dark cycle) and maintained with standard lab chow (pellet diet) and water ad libitum unless otherwise noted. All surgical and experimental procedures were approved by the Institutional Animal Care and Use Committee (IACUC) at Seoul National University. This study conformed to the ARRIVE (Animal Research: Reporting In Vivo Experiments) guidelines for preclinical animal studies.

## *Behavioral test for Masticatory efficiency*

All mice were fasted 24 hours and habituated for an hour in a clear acrylic cage (8.5 cm in length, 8.5 cm in width, and 17 cm in height) before the behavioral test. Mice body weight was measured before the habituation period. Chow was wrapped in an aluminum foil so that only 1-cm of chow was exposed and then attached inside the acrylic cage 2.5 cm above the ground to limit approach regions for clear discrimination of chow consumption behavior. After habituation, animals were exposed to chow for free consumption and this was recorded with a video camera for an hour. The chow approaching number was defined as the sum of the individual event that the mouse approached and masticated the chow. The chow approaching time was defined as the total time the mouse spent on feeding chow. Chow weight was measured again after the behavioral test to obtain the chow consumption weight by subtracting the chow weight measured prior to the test. The chow consumption weight was divided by

the body weight measured before the test to minimize the individual variation between the mice. The maximal biting force of the mice was recorded with a Piezo sensor (FlexiForce, A201, Tekscan, USA) by mildly restraining the mouse with hand for free head movement and placing the tip of the Piezo sensor in front of the snout for biting with incisors. The biting force was measured for 200 seconds per mouse, and the data was transformed in numerical value by FlexiForce software (FlexiForce, A201, Tekscan, USA). The maximal biting force was determined from the highest score.

### ***Rotarod test***

Rotarod test protocol was modified from the rat protocol (Singh et al. 2018). Motor coordination of the mice were measured with rotarod test apparatus (Rotamax-5 1.3, Columbus Instruments, USA). Mice were placed on the rotating horizontal bar (6-cm diameter) with a starting speed of 4 revolutions per minute (RPM) with 1 RPM acceleration every 8 seconds. Mice were trained on the apparatus twice prior to the test.

### ***Sample preparation for histology***

Animals were anaesthetized after the behavioral experiments by pentobarbital (80 mg/kg, i.p. injection) and perfused with phosphate-buffered saline (PBS) and fixed with 4% paraformaldehyde (PFA). The brainstem region tissues were harvested, post-fixed overnight in 4% PFA at 4°C, and cryoprotected with 30% sucrose in PBS. After the cryoprotection, the tissues were embedded in O.C.T compound (Scigen, 4586) and snap-frozen with liquid nitrogen. Brain tissues were transversely sectioned at 40 µm per section. Masseter muscle, hyoglossus muscle, and posterior belly of digastric muscle that were vertically

sectioned at 14  $\mu$ m.

### ***Immunohistochemistry***

Brainstem sections were blocked for 2 hours at room temperature with 4% normal horse serum in 0.3% Triton-X in PBS (PBST), and then incubated with primary antibodies: mouse anti-A $\beta$  monoclonal antibody (4G8, 1:500, #SIG-39220, BioLegend), goat anti-choline acetyltransferase (ChAT, 1:500, #AB144P, Merck Millipore), rabbit anti-cleaved caspase-3 (cas-3, 1:500, #9664, Cell Signaling Technology), and rabbit anti-Iba-1 (Iba-1, 1:500, 019-19741, FujiFilm) in 4% normal horse serum in 0.3% PBST for 2 days at room temperature. The sections were washed with PBS three times, and then incubated with secondary antibodies: donkey anti-goat cy3 (1:250, #705-165-147, Jackson), donkey anti-rabbit cy3 (1:250, #711-165-152, Jackson), and donkey anti-mouse Alexa Fluor 488 (1:250, #715-545-150, Jackson) in 0.3% PBST for 2h at room temperature. For the A $\beta$  plaque staining, 1% Thioflavin S (1%, T-1892, Sigma) in PBS was applied for 12 minutes and then washed three times with PBS.

Muscle sections were blocked with 2% normal horse serum in 0.3% PBST for 2h and incubated with rabbit anti-laminin polyclonal antibody (1:500, ab11575, Abcam) in 2% normal horse serum in 0.3% PBST for 48h at room temperature. The sections were washed three times with PBS and incubated with donkey anti-rabbit Alexa Fluor 488 (1:500, #711-545-152, Jackson) in 0.3% PBST for 2h at room temperature.

All sections were mounted with coverslips, examined by LSM 700 confocal microscope (Zeiss), and analyzed with Zen blue lite edition and ImageJ.

### ***Image analysis and quantification***

The sections for brainstem regions were obtained according to brain coordinates relative to bregma -4.84 to -7.48 mm. Each section was collected in order from rostral to caudal and mounted every 80 $\mu$ m. The region of interest (ROI) and borders for subnucleus were selected according to Allen brain atlas, using imaging processing software (ZEN 3.2 Blue, Zeiss). For each immunostained coronal section, the number of Thioflavin+ plaques, ChAT+ neuronal cells, and the overlap ratio were counted manually. The density of plaque/cells was calculated based on the area of ROI, provided by the software imageJ. For each mouse, 5 transverse sections of hyoglossus and posterior belly of digastric muscle were acquired and analyzed with ImageJ. From each image, area of muscle fiber was automatically measured using particle analysis in ImageJ.

For masseter muscle size measurement, coronal sections of masseter muscle were laminin-stained to distinguish the boundary of a single muscle fiber. Contents of a laminin-stained boundary were considered as a single muscle fiber and each area of the fiber was measured by ImageJ particle analysis function. To estimate the diameter of the muscle fiber, each fiber was assumed to have circular shape. Diameters were calculated by dividing the square root of the inner space area of the laminin-stained boundary by  $\pi$  (the ratio of the circumference of a circle to its diameter). The obtained fiber diameter was aligned with a width of 5  $\mu$ m to compare size distributions of the muscle fiber.

#### ***H&E staining of mandibular masseter muscle***

The sample was fixed with formalin and sequentially dehydrated with 80-100% ethanol in increasing alcohol concentration. The tissues were then infiltrated with resin (Technovit 7200, Heraeus Kulzer GmbH, Germany). The solidified blocks were made by using a foaming agent and light curing unit

(EXAKT, Germany). The tissue blocks were attached to the acrylic mold, cut, and ground with a cutting and grinding machine (EXAKT, Germany) to the desired thickness for H&E staining. All sections were imaged with a light microscope (Leica, Germany), and analyzed with ImageJ.

### ***MicroCT***

The head specimens of 5XFAD and littermates were sagittally split into two symmetrical parts, which were then post-fixed in 4% PFA (pH 7.4) at 4°C for 48h. They were further kept in 70% ethanol at 4°C until the day of microCT scanning. Scanning of the mandibular first molar of 5XFAD mice and littermate mice was performed by Skyscan 1172 (Bruker, Kontich, Belgium). The scanning parameters were 6.92µm pixel size, 70kV X-ray voltage, 141µA electric current, and 0.5mm Al filter. All data sets were reconstructed with NRecon software (SkyScan, Aartselaar, Belgium). Using the protocol modified from the quantitative analysis of rat jawbone microstructures (Chatterjee et al. 2017), volume of the whole first molar, crown, and canal from each genotype were analyzed by CT Analyzer (CTAn, version 1.18.8.0, Bruker).

### ***Statistical Analysis***

All statistics were performed by Prism software (version 6.01). Comparison between multiple groups was made by one-way analysis of variance (ANOVA) with Bonferroni post-hoc test, and comparison between two groups were made using the Student's t-test. Differences with p values < 0.05 were regarded as statistically significant.

# RESULTS

## **5XFAD mice showed decreased masticatory function**

I used 5-months-old 5XFAD mice when the animals are known to have cognitive impairment (Lewis et al. 2006). I first examined the masticatory efficiency of 5XFAD mice by measuring the chow consumption behavior after 24-hour fasting. There was no difference in chow consumption between 5XFAD and littermate mice (**Fig. 14B**), but the total time spent for chow feeding behavior and the total number of approaches were significantly increased in the 5XFAD compared to the littermate mice (**Fig. 14C, 14D**). Next, I compared the maximal biting force, and 5XFAD mice showed significantly decreased maximal biting force compared to the littermate (**Fig. 14E**). However, when I measured general motor activity of the mice by the rotarod performance test, there was no difference in the retention time between the groups (**Fig. 14F**).

## **A $\beta$ accumulated specifically in the trigeminal motor nucleus in 5XFAD mice**

I then investigated the A $\beta$  accumulation in various cranial motor nuclei, such as the trigeminal motor nucleus (Vmo) that directly innervates to the masticatory muscle, the facial motor nucleus (7th cranial motor nucleus) and the hypoglossal motor nucleus (12th cranial motor nucleus) that are involved in the movement of the orofacial region, and the dorsal motor nucleus of the vagus nerve (10th cranial motor nucleus) as the control cranial motor nucleus (Nakamura et al. 2004). I identified motor neurons with cholinergic neuronal marker (ChAT), and A $\beta$  accumulation was determined by immunostaining with anti-A $\beta$  17-24 antibody (clone 4G8) (Toussey et al. 2015) and Thioflavin S

fluorescent dye for targeting A $\beta$  plaque (Yuan and Grutzendler 2016). The staining showed a distinct accumulation of A $\beta$  plaque in ChAT-positive area of Vmo compared to the other cranial nuclei (**Fig. 15A-C**). We further examined A $\beta$  plaque accumulation in the subregions of Vmo, ventromedial Vmo (VM Vmo, jaw-opening muscle) and dorsolateral Vmo (DL Vmo, jaw-closing muscle), and observed significantly increased A $\beta$  plaque accumulation in the DL Vmo compared to VM Vmo (**Fig. 16A, 16B**).

### **Preferential microglial activation and cell death of trigeminal motor nucleus in 5XFAD mice**

Since toxic A $\beta$  oligomers have been proposed to cause brain inflammation and neuronal degeneration (Butterfield and Lashuel 2010; Grimaldi et al. 2018), I next examined the microglial activation and cell death of Vmo neurons in 5XFAD mice. Consistent with A $\beta$  accumulation in Vmo, I observed an increased number of microglia in the Vmo compared to the other nuclei in the 5XFAD mice (**Fig. 17A, 17B**). The percentage of activated microglia with de-ramification and swelling of the cell body (**Fig. 17C**) was also significantly increased in the Vmo compared to the other nuclei (**Fig. 17D**). The number of activated microglia in the Vmo was also significantly increased in the 5XFAD mice compared to the littermate mice (**Fig. 17E**). To confirm the neuronal degeneration of Vmo, I analyzed immunoreactive cells with active caspase-3, a cell death marker, which were found only in the Vmo of the 5XFAD mice (**Fig. 17F**). The number of ChAT-positive cells was significantly decreased in the 5XFAD mice compared to the littermate (**Fig. 17G**), whereas the total size of the Vmo did not differ between two groups (**Fig. 17H**).



### **Masseter muscle weight and fiber thickness were decreased in 5XFAD mice**

Finally, I investigated the changes of the masticatory muscle innervated by the Vmo neurons, and observed significant decrease in both weight (**Fig. 18A**) and area (**Fig. 18B, 18C**) of masseter muscle in the 5XFAD mice compared to the littermate. The thickness of masseter muscle fiber was also significantly decreased in 5XFAD compared to the littermate, thereby shifting left to the smaller size in the proportion of muscle fiber size (**Fig. 18D-18F**). However, when I further compared the fiber size of the muscles innervated by other cranial nuclei, both posterior belly of the digastric muscle innervated by the facial motor nucleus (**Fig. 19A, 19B**) and hyoglossus muscle innervated by the hypoglossal nucleus (**Fig. 19C, 19D**) showed no difference in average muscle fiber size between 5XFAD and littermate mice. To further investigate the changes in masticatory system components other than the muscle, I measured volumetric changes in various components of the mandibular first molar (**Fig. 20A**). The crown, root, and the whole volume of the first molar showed no significant difference between two groups (**Fig. 20B-D**).

Figure 14

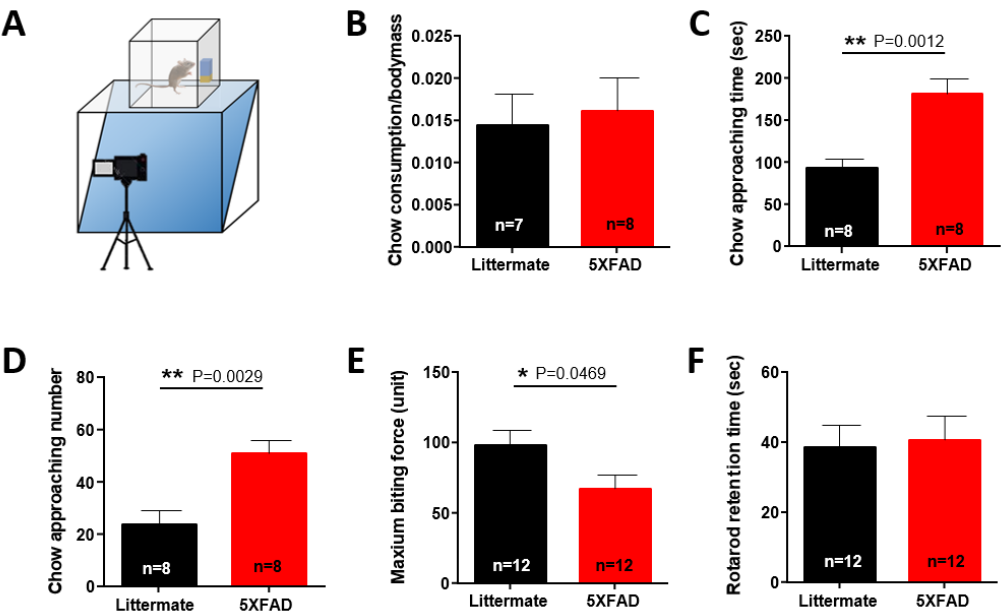


## **Figure 14. Measurement of masticatory efficiency in 5XFAD mice.**

(A) Graphical illustration of chow consumption behavior test. (B) Weight of chow fed by mice were divided by body weight of the individual mice before the experiment ( $n = 8/\text{group}$ ,  $P = 0.4153$ ), (C) Total time spent for chow feeding ( $n = 8/\text{group}$ ,  $**P = 0.0012$ ) and (D) Chow approaching number ( $n = 8/\text{group}$ ,  $**P = 0.0029$ ). (E) Maximal biting force (5XFAD;  $n = 9$ , Littermate;  $n = 10$ ,  $*P = 0.0469$ ) and (F) Rotarod body performance test ( $n = 12/\text{group}$ ). (B-F) The 5XFAD mice versus its littermate controls. Mean  $\pm$  SEM.  $**P < 0.01$ ;  $*P < 0.05$

Figure 15

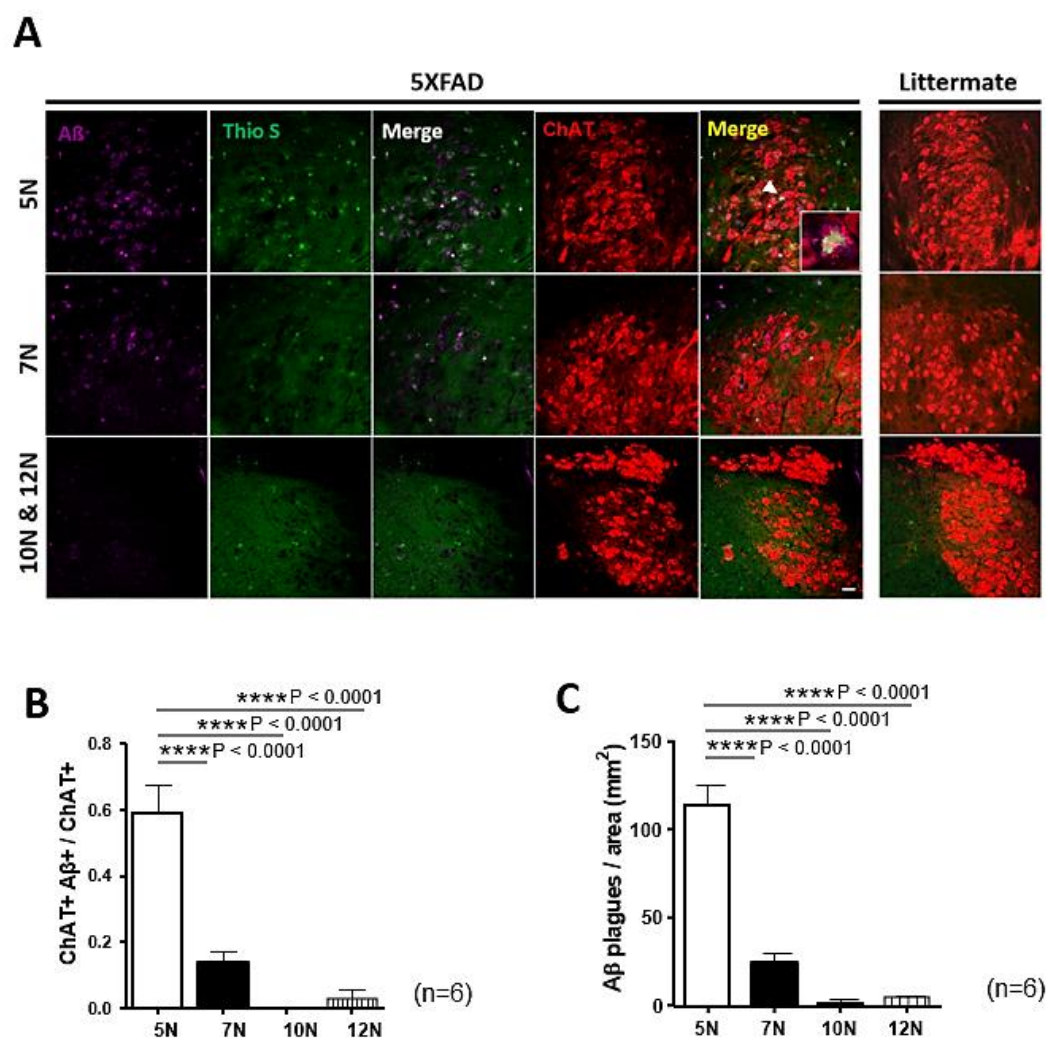


## **Figure 15. A $\beta$ accumulation in cranial motor nuclei of 5XFAD mice.**

(A) Staining of A $\beta$  (Purple), Thioflavin S (Green) and ChAT (Red). Arrowhead (white) indicates co-localization of ChAT, Thioflavin S and A $\beta$  staining. Squarebox showing zoomed in image of arrowhead region. and scale bar (white); 50 $\mu$ m. (B) Quantitative data showing ratio of A $\beta$ <sup>+</sup> ChAT<sup>+</sup> neurons (One-way ANOVA:  $F(3,20) = 83.35$ ,  $P < 0.0001$  with Bonferroni post-test, Mean  $\pm$  SEM. \*\*\*\* $P < 0.0001$ ; \*\*\* $P < 0.001$ ;  $n = 6$  mice/group) (C) Number of A $\beta$  plaque in ChAT<sup>+</sup> area from cranial nuclei (5N, 7N, 10N and 12N). Trigeminal motor nucleus (Vmo); 5N, Facial motor nucleus; 7N, Vagus nucleus; 10N, Hypoglossal nucleus; 12N. One-way ANOVA:  $F(3,20) = 67.24$ ,  $P < 0.0001$  with Bonferroni post-test, Mean  $\pm$  SEM. \*\*\*\* $P < 0.0001$ ; \*\*\* $P < 0.001$ ;  $n = 6$  mice/group).

### Figure 16

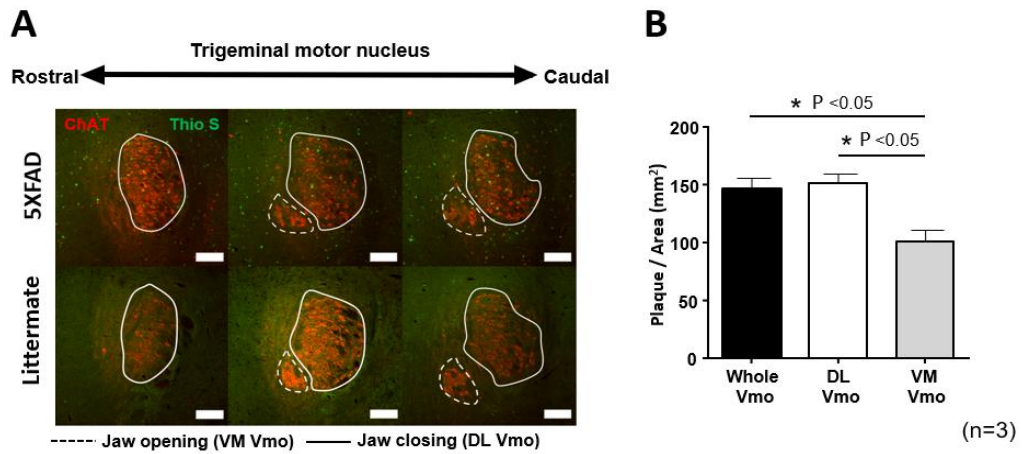


**Figure 16. A $\beta$  accumulation in ventromedial and dorsolateral division of cranial motor nuclei of 5XFAD mice.**

(A) Staining of Thioflavin S (Green) and ChAT (Red) in rostral to caudal Vmo. Dotted line (white) represents ventromedial (VM) Vmo region innervating jaw opening muscle and solid line (white) represents dorsolateral (DL) Vmo region innervating jaw closing muscle. Scale bar (white); 200 $\mu$ m. (B) Number of A $\beta$  plaque in ChAT+ area from whole Vmo, VM Vmo and DL Vmo. One-way ANOVA:  $F(2,6) = 9.231$ ,  $P = 0.0148$  with Bonferroni post-test, Mean  $\pm$  SEM. \*\*\*\* $P < 0.0001$ ; \*\*\* $P < 0.001$ ;  $n = 3$  mice/group).

Figure 17

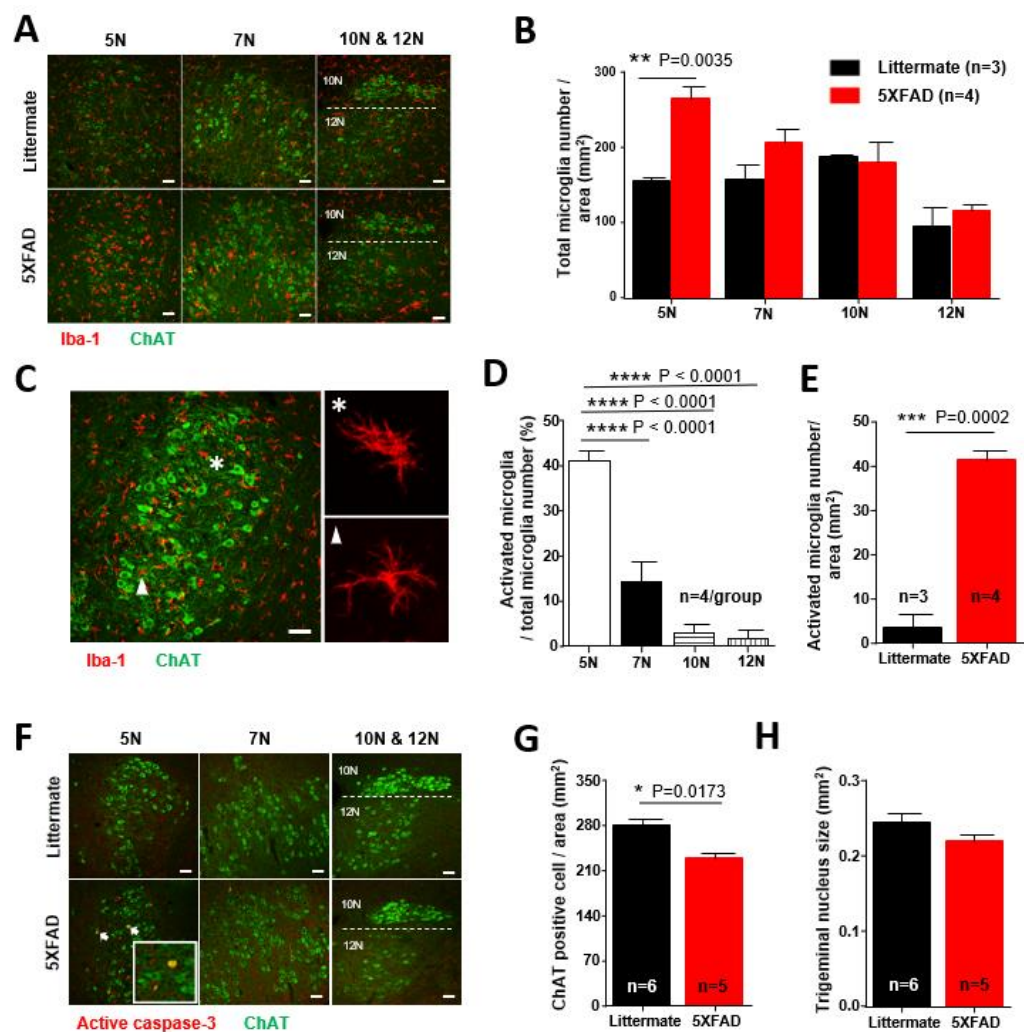




## **Figure 17. Brain inflammation and cell death in the cranial motor nuclei of 5XFAD mice.**

(A) Immunostaining of ChAT (Green) and Iba1 (Red). Scale bar (white); 50 $\mu$ m. (B) Total number of microglia/area (mm<sup>2</sup>) (n = 3, Littermate; n = 4, 5XFAD). (C) Immunostaining of microglia in 5N, activated (asterisk) and deactivated form of microglia (arrowhead). Scale bar (white); 50 $\mu$ m. (D) Percentage of activated microglia to the total number of microglia in 5N, 7N, 10N and 12N. One-way ANOVA:  $F(3,12) = 46.33$ ,  $P < 0.0001$  with Bonferroni post-test, Mean  $\pm$  SEM. \*\*\*\* $P < 0.0001$ ; \*\*\* $P < 0.001$ ; n = 4/group). (E) Activated microglia per area unit (mm<sup>2</sup>) (Mean  $\pm$  SEM. Student's t-test,  $P = 0.0002$ , n = 3, Littermate; n = 4, 5XFAD). (F) Staining of ChAT (Green) and caspase-3 (Red). Chat+ and caspase-3+ cells are presented in arrows. Scale bar (white); 50 $\mu$ m. (G) Number of ChAT+ cells per area unit (mm<sup>2</sup>) in 5N and (H) Size of the 5N (mm<sup>2</sup>). Trigeminal motor nucleus; 5N, Facial motor nucleus; 7N, Vagus nucleus (dorsal-motor); 10N, Hypoglossal nucleus; 12N. Mean  $\pm$  SEM. Student's t-test, \*\*\*\* $P < 0.0001$ ; \*\*\* $P < 0.001$ ; \*\* $P < 0.01$ ; \* $P < 0.05$

**Figure 18.**

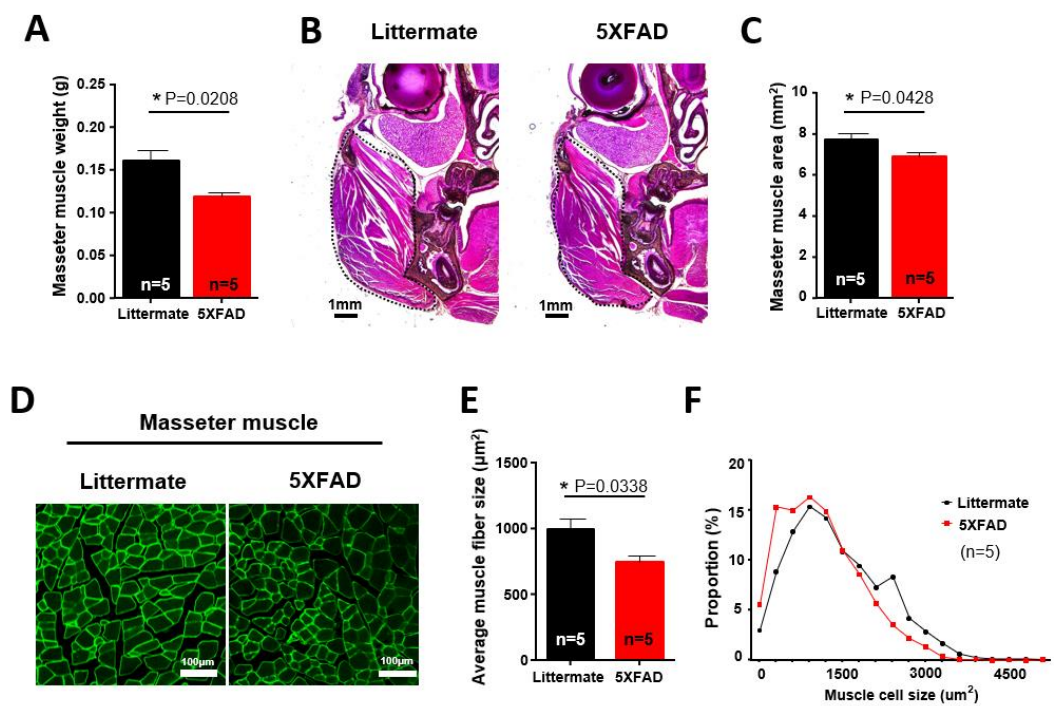


**Figure 18. Histological characterization of masseter muscle in 5XFAD mice.**

(A) Masseter muscle weight ( $n = 5/\text{group}$ ,  $*P = 0.0208$ ), (B) H&E staining of whole maxillary and mandibular coronal section and (C) Masseter muscle area ( $n = 5/\text{group}$ ,  $*P = 0.0428$ ). (D) Representative image of cross section of masseter muscle stained with laminin (green). (E) Bar graph analysis of masseter muscle fiber diameter ( $n = 5/\text{group}$ ,  $*P = 0.0338$ ) and (F) Size distribution of masseter muscle fiber diameter. MicroCT image and (G) 3-D volumetric measurements of crown (H), tooth root (I) and whole first mandibular molars (J) in 5XFAD mice and littermate ( $n = 7$  mice/group). All data presented in mean  $\pm$  SEM. Student's t-test,  $**P < 0.01$ ;  $*P < 0.05$ .

**Figure 19.**

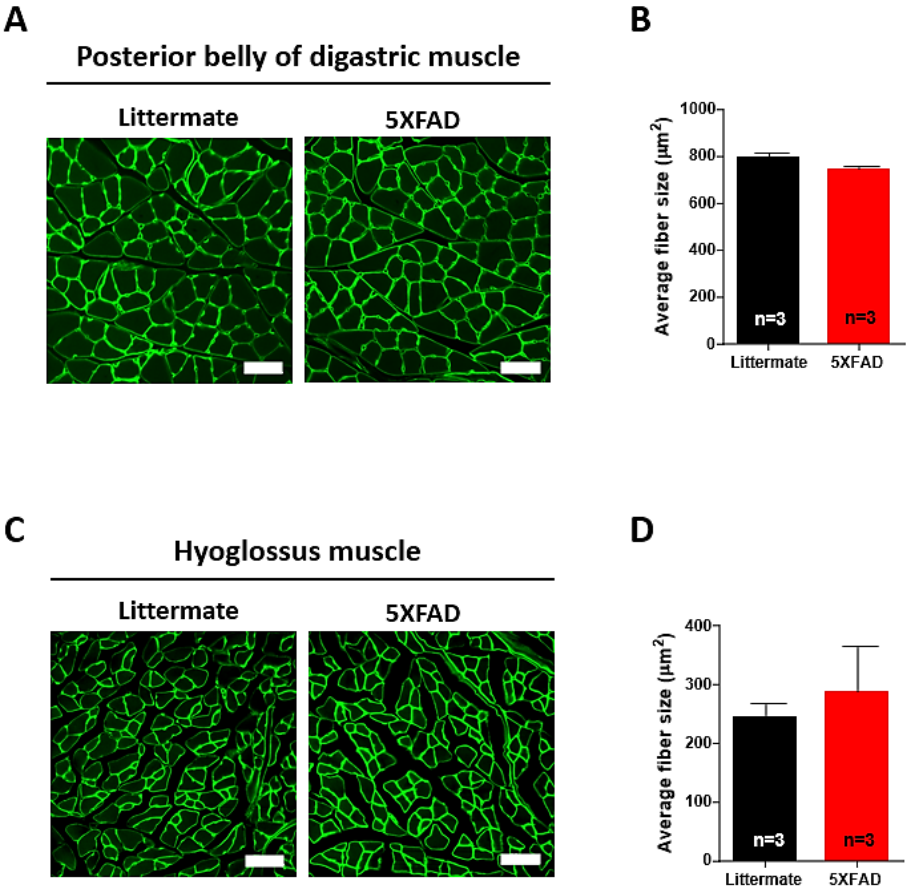


**Figure 19. Histological analysis of the digastric muscle and hyoglossus muscle of 5XFAD mice.**

(A) Representative immunohistochemistry image of digastric muscle cross-section of littermate (Left) and 5XFAD mice (Right), stained with laminin (green). Scale bar, 50 $\mu$ m. (B) Bar graph analysis of posterior belly of digastric muscle fiber cross-section area (n = 3/group, P = 0.1754). All data presented in Mean  $\pm$  SEM. Student's t-test. (C) Representative immunohistochemistry image of hyoglossus muscle cross-section of littermate (Left) and 5XFAD mice (Right), stained with laminin (green). Scale bar, 50 $\mu$ m. (D) Bar graph analysis of hyoglossus muscle fiber cross-section area (n = 3/group, P = 0.6278). All data presented in Mean  $\pm$  SEM. Student's t-test.

**Figure 20.**

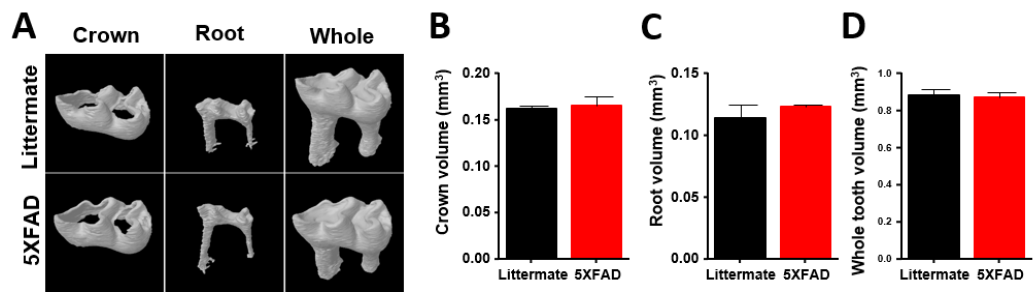


**Figure 20. Volumetric analysis of the mouse first molar in 5XFAD mice.**

MicroCT image (A) and 3-D volumetric measurements of crown (B), tooth root (C) and whole first mandibular molars (D) in 5XFAD mice and littermate (n = 7 mice/group). All data presented in mean  $\pm$  SEM. Student's t-test, \*\*P < 0.01; \*P < 0.05.

## DISCUSSION

In this study, I found decreased masticatory efficiency and maximum biting force in 5XFAD mice, without a significant change in general motor function. Excessive accumulation of A $\beta$ , increased number of microglia and regional cell death were also observed in Vmo, which innervates to jaw-closing masseter muscle, in comparison to the other cranial motor nuclei. Furthermore, the weight and muscle fiber size of masseter muscle, but not of posterior belly of the digastric muscle and hyoglossus muscle, were significantly decreased in 5XFAD mice, compared with its littermates. These results suggest a correlation of specific A $\beta$  accumulation in Vmo with masticatory dysfunction in Alzheimer's disease.

I first examined the outcome of significant A $\beta$  accumulation in VMO in the masticatory function with sets of behavioral tests. The mastication efficiency was measured when mastication naturally occurs. Although the chow intake did not differ between the groups, 5XFAD mice showed increased total time spent for chow feeding and in number of feeding behavior (**Fig. 14B-D**). These results indicate that 5XFAD mice may have decreased masticatory efficiency, which is consistent with the clinical research showing functional decline of mastication such as increased masticatory cycle time, slow masticatory velocity, and decreased biting force in AD patients (Karlsson and Carlsson 1990). The biting force was also decreased in 5XFAD mice, indicating the disrupted masticatory function (**Fig. 14D**). Interestingly, there was no difference in rotarod retention time between 5XFAD and littermates (**Fig. 14E**), which is consistent with a recent report showing no cell deaths observed in the motor neuron of cervical spinal cord of 6-months-old 5XFAD mice compared to non-transgenic littermates



(Chu et al. 2017). These results suggest that masticatory dysfunction seen in 5-month-old 5XFAD mice occurs prior to cerebellar or spinal cord degeneration.

A $\beta$ , the pathological hallmark of AD, is highly correlated with the pathological process of neural degeneration. The regional profile of A $\beta$  accumulation in brain structures has been studied with the purpose of interpreting functional alteration and progression of the disease stage. For example, A $\beta$  accumulation in cortical regions and hippocampus has been implicated in cognitive deficiency and decreased function of spatial memory (Lewis et al. 2006). Furthermore, several studies have shown that olfactory malfunction in AD is caused by A $\beta$  accumulation in the somatostatin-positive neuronal population of the olfactory bulb (Meshulam et al. 1998; Yoo et al. 2017). In agreement with the study which reported the A $\beta$  accumulation in Vmo of 3xTGAD mice (Overk et al. 2009), my result demonstrated specific accumulation of A $\beta$  and plaque formation in Vmo (**Fig. 15**). It was interesting to note that A $\beta$  accumulation in other cranial motor nuclei that innervate the orofacial region was relatively limited, and when I compared DL Vmo (which innervates jaw-closing muscle) and VM Vmo (which innervates jaw-opening muscle) (Travers 2015), A $\beta$  plaque accumulation was significantly higher in DL Vmo than VM Vmo (**Fig. 16**). A degenerative event like brain inflammation with microglial activation and caspase-3 expression, was also consistently present with A $\beta$  accumulation (**Fig. 17**). Although there is a lack of direct clinical evidence showing the accumulation of A $\beta$  in Vmo, the possibility of occasional A $\beta$  accumulation in Vmo due to increased expression and extensive colocalization of APP and calpain-I remains high (Siman et al. 1990).

Given the degeneration of Vmo neurons, my final question was whether Vmo degeneration is accompanied by any impairments of the peripheral

masticatory system. My results showed decreased masseter muscle weight and atrophy based on the histological analysis (**Fig. 18A-F**). Recently, a study in DstGt homozygous mice (model of sensory and autonomic neuropathy type VI) showed cell death in Vmo motoneurons with masseter muscle atrophy and weak activity of electromyography (Hossain et al. 2018). This phenomenon could be interpreted from a study showing muscle weakness caused by denervation of motoneuron and presynaptic dysfunction of the neuromuscular junction (Kong et al. 2009). In addition, A $\beta$  is known to produce cytotoxic effects and attenuate excitatory synaptic transmission (Karlsson and Carlsson 1990; Terry et al. 1991). Taken together, A $\beta$  accumulation in Vmo neurons may lead to neuronal cell death that decreases the innervation of motoneurons to masseter muscle or disrupts presynaptic modulations that alter the muscle morphology. Given the less or no accumulation of A $\beta$  in facial nucleus and hypoglossal nucleus, both posterior belly of the digastric muscle and hyoglossus muscle which are innervated by each nucleus was comparable in fiber size between 5XFAD and littermate mice (**Fig. 19**).

In conclusion, specific accumulation of A $\beta$  in Vmo is strongly associated with decreased masticatory efficiency in 5XFAD mice. This may explain the masticatory dysfunction seen in AD patients, suggesting a close relationship between mastication and AD.

## GENERAL DISCUSSION

Sensory and motor abnormalities are abundantly found in neurological disorders such as pain and Alzheimer's disease. However, research on therapeutic target and the characterization of target pathway is still limited. Therefore, investigation of mechanism of peripheral sensory and motor abnormalities on neurological disorders are required for development of treatment target and management of symptoms. In this thesis, I have investigated the effect of mycolactone and its following mechanism of action in the sensory neurons. Also, trigeminal motor pathologies in Alzheimer's disease.

In the first chapter, I demonstrated the analgesic effect of the mycolactone in various pain models which may produce analgesia by inducing hyperpolarization in DRG neurons through the AT2R pathway without toxicity. Furthermore, I successfully miniaturized and developed phenotypic cellular assay and validated mechanism following AT2R pathway mycolactone induce hyperpolarization in DRG sensory neurons. In addition, the co-incubation of AT2R ligands with mycolactone did not affect the hyperpolarization mediated by mycolactone. The results from chapter I indicate that bacterial products such as mycolactone can target sensory abnormality such as pathological pain and can have potential therapeutic effects activating non-conventional pathways. However, it is yet to be known whether mycolactone can have greater efficacy and less side effect in pain management than conventional pain treatments such as gabapentin, opioids and NSAIDs. Therefore, further research is needed regarding the efficacy and side effect in the use of mycolactone as an analgesic compound. Also, as mycolactone activates AT2R pathway, it may have similar effect on other cell types such as macrophages or T-cells. Therefore, *in vivo* and

*in vitro* study on the effect of mycolactone on neuro-immune interaction is needed for further explore the mechanism of analgesia induced by mycolactone.

In the second chapter, I found decreased masticatory efficiency and maximum biting force in 5XFAD mice, without a significant change in general motor function. Excessive accumulation of A $\beta$ , increased number of microglia and regional cell death were also observed in Vmo, which innervates to jaw-closing masseter muscle, in comparison to the other cranial motor nuclei. The outcome of the central A $\beta$  pathology extends to the peripheral masticatory system which is demonstrated by the decreased weight and muscle fiber size of masseter muscle in 5XFAD AD model mice. This results strongly support the correlation between regional A $\beta$  accumulation in the brainstem governing mastication and the degeneration of the peripheral motor system and its activity. However, there are several limitations to the research as it is yet to be discussed whether masticatory dysfunction can be found before the cognitive decline in AD model mice. Therefore, a further study is needed for distinguish the timepoint of onset in which peripheral masticatory dysfunction occurs behaviorally and histologically. On the other hand, it is also essential to find out whether the continuous input of the masticatory stimulus can reverse or delay the onset of the cognitive degeneration in AD model mice. It is also important to validate the histological changes in human AD brain as the use of mice model may not fully reflect pathological changes found in human. However, the successful development of the behavioral managing scheme and the histological validation in AD mice model may provide insight on the novel AD treatment and diagnostic interventions.

## REFERENCES

- Adusumilli S, Mve-Obiang A, Sparer T, Meyers W, Hayman J, Small PLC. 2005. Mycobacterium ulcerans toxic macrolide, mycolactone modulates the host immune response and cellular location of m. Ulcerans in vitro and in vivo. Cellular microbiology. 7(9):1295-1304.
- Albers MW, Gilmore GC, Kaye J, Murphy C, Wingfield A, Bennett DA, Boxer AL, Buchman AS, Cruickshanks KJ, Devanand DP. 2015. At the interface of sensory and motor dysfunctions and alzheimer's disease. Alzheimer's & Dementia. 11(1):70-98.
- Anand U, Facer P, Yiangou Y, Sinisi M, Fox M, McCarthy T, Bountra C, Korchev Y, Anand P. 2013. Angiotensin ii type 2 receptor (at2r) localization and antagonist-mediated inhibition of capsaicin responses and neurite outgrowth in human and rat sensory neurons. European journal of pain. 17(7):1012-1026.
- Anand U, Sinisi M, Fox M, MacQuillan A, Quick T, Korchev Y, Bountra C, McCarthy T, Anand P. 2016. Mycolactone-mediated neurite degeneration and functional effects in cultured human and rat drg neurons: Mechanisms underlying hypoalgesia in buruli ulcer. Molecular Pain. 12:1744806916654144.
- Baron L, Paatero AO, Morel J-D, Impens F, Guenin-Macé L, Saint-Auret S, Blanchard N, Dillmann R, Niang F, Pellegrini S. 2016. Mycolactone subverts immunity by selectively blocking the sec61 transloconimmunity lost in translocation. The Journal of experimental medicine. 213(13):2885-2896.
- Benitez S, Seltzer A, Acosta C. 2017. Nociceptor-like rat dorsal root ganglion neurons express the angiotensin-ii at2 receptor throughout development. International Journal of Developmental Neuroscience. 56:10-17.
- Bennett GJ, Xie Y-K. 1988. A peripheral mononeuropathy in rat that produces disorders of pain sensation like those seen in man. Pain. 33(1):87-107.
- Bieri R, Scherr N, Ruf M-T, Dangy J-P, Gersbach P, Gehringer M, Altmann K-H, Pluschke G. 2017. The macrolide toxin mycolactone promotes bim-dependent apoptosis in buruli ulcer through inhibition of mtor. ACS chemical biology. 12(5):1297-1307.
- Borsook D. 2012. Neurological diseases and pain. Brain. 135(2):320-344.
- Cadaveira-Mosquera A, Ribeiro SJ, Reboreda A, Pérez M, Lamas JA. 2011. Activation of trek currents by the neuroprotective agent riluzole in mouse sympathetic neurons. Journal of Neuroscience. 31(4):1375-1385.

- Campos CH, Ribeiro GR, Costa JL, Rodrigues Garcia RC. 2017. Correlation of cognitive and masticatory function in alzheimer's disease. *Clin Oral Investig.* 21(2):573-578.
- Dangy J-P, Scherr N, Gersbach P, Hug MN, Bieri R, Bomio C, Li J, Huber S, Altmann K-H, Pluschke G. 2016. Antibody-mediated neutralization of the exotoxin mycolactone, the main virulence factor produced by mycobacterium ulcerans. *PLOS Neglected Tropical Diseases.* 10(6):e0004808.
- Demangel C, Stinear TP, Cole ST. 2009. Buruli ulcer: Reductive evolution enhances pathogenicity of mycobacterium ulcerans. *Nature Reviews Microbiology.* 7(1):50-60.
- Farquhar-Smith WP. 2008. Anatomy, physiology and pharmacology of pain. *Anaesthesia & intensive care medicine.* 9(1):3-7.
- Feng Y, Mitchison TJ, Bender A, Young DW, Tallarico JA. 2009. Multi-parameter phenotypic profiling: Using cellular effects to characterize small-molecule compounds. *Nature Reviews Drug Discovery.* 8(7):567-578.
- Fenistein D, Lenseigne B, Christophe T, Brodin P, Genovesio A. 2008. A fast, fully automated cell segmentation algorithm for high-throughput and high-content screening. *Cytometry Part A: the journal of the International Society for Analytical Cytology.* 73(10):958-964.
- Frost S, Martins RN, Kanagasalingam Y. 2010. Ocular biomarkers for early detection of alzheimer's disease. *J Alzheimers Dis.* 22(1):1-16.
- George KM, Chatterjee D, Gunawardana G, Welty D, Hayman J, Lee R, Small P. 1999. Mycolactone: A polyketide toxin from mycobacterium ulcerans required for virulence. *Science.* 283(5403):854-857.
- Guenin-Macé L, Veyron-Churlet R, Thoulouze M-I, Romet-Lemonne G, Hong H, Leadlay PF, Danckaert A, Ruf M-T, Mostowy S, Zurzolo C. 2013. Mycolactone activation of wiskott-aldrich syndrome proteins underpins buruli ulcer formation. *The Journal of clinical investigation.* 123(4):1501-1512.
- Hall BS, Hill K, McKenna M, Ogbechi J, High S, Willis AE, Simmonds RE. 2014. The pathogenic mechanism of the mycobacterium ulcerans virulence factor, mycolactone, depends on blockade of protein translocation into the er. *PLoS Pathog.* 10(4):e1004061.
- He Z, Guo JL, McBride JD, Narasimhan S, Kim H, Changolkar L, Zhang B, Gathagan RJ, Yue C, Dengler C. 2018. Amyloid- $\beta$  plaques enhance alzheimer's brain tau-seeded pathologies by facilitating neuritic plaque tau aggregation. *Nature medicine.* 24(1):29.

- Hein L, Barsh GS, Pratt RE, Dzau VJ, Kobilka BK. 1995. Behavioural and cardiovascular effects of disrupting the angiotensin ii type-2 receptor gene in mice. *Nature*. 377(6551):744-747.
- Hylands-White N, Duarte RV, Raphael JH. 2017. An overview of treatment approaches for chronic pain management. *Rheumatology international*. 37(1):29-42.
- Johnson KA, Fox NC, Sperling RA, Klunk WE. 2012. Brain imaging in alzheimer disease. *Cold Spring Harbor Perspectives in Medicine*. 2(4):a006213-a006213.
- Juárez-Contreras R, Rosenbaum T, Morales-Lázaro SL. 2018. Lysophosphatidic acid and ion channels as molecular mediators of pain. *Frontiers in Molecular Neuroscience*. 11.
- Krames ES. 1999. Interventional pain management: Appropriate when less invasive therapies fail to provide adequate analgesia. *Medical Clinics of North America*. 83(3):787-808.
- Lewis H, Beher D, Cookson N, Oakley A, Piggott M, Morris CM, Jaros E, Perry R, Ince P, Kenny RA et al. 2006. Quantification of alzheimer pathology in ageing and dementia: Age-related accumulation of amyloid-beta(42) peptide in vascular dementia. *Neuropathol Appl Neurobiol*. 32(2):103-118.
- Marion E, Prado S, Cano C, Babonneau J, Ghamrawi S, Marsollier L. 2012. Photodegradation of the mycobacterium ulcerans toxin, mycolactones: Considerations for handling and storage. *PLoS One*. 7(4):e33600.
- Marion E, Song O-R, Christophe T, Babonneau J, Fenistein D, Eyer J, Letournel F, Henrion D, Clere N, Paille V. 2014. Mycobacterial toxin induces analgesia in buruli ulcer by targeting the angiotensin pathways. *Cell*. 157(7):1565-1576.
- Marsollier L, Brodin P, Jackson M, Korduláková J, Tafelmeyer P, Carbonnelle E, Aubry J, Milon G, Legras P, Saint André J-P. 2007. Impact of mycobacterium ulcerans biofilm on transmissibility to ecological niches and buruli ulcer pathogenesis. *PLoS Pathog*. 3(5):e62.
- Marsollier L, Robert R, Aubry J, Saint André J-P, Kouakou H, Legras P, Manceau A-L, Mahaza C, Carbonnelle B. 2002. Aquatic insects as a vector for mycobacterium ulcerans. *Applied and environmental microbiology*. 68(9):4623-4628.
- Martini F. 2006. *Anatomy and physiology*'2007 ed. Rex Bookstore, Inc.
- Meshulam RI, Moberg PJ, Mahr RN, Doty RL. 1998. Olfaction in neurodegenerative disease: A meta-analysis of olfactory functioning in alzheimer's and parkinson's diseases. *Arch Neurol*. 55(1):84-90.

- Meyin A Ebong S, Petit E, Le Gall P, Chen P-P, Nieser N, Guilbert E, Njiokou F, Marsollier L, Guégan J-F, Pluot-Sigwalt D. 2016. Molecular species delimitation and morphology of aquatic and sub-aquatic bugs (heteroptera) in cameroon. *PloS one*. 11(5):e0154905.
- Moffat JG, Vincent F, Lee JA, Eder J, Prunotto M. 2017. Opportunities and challenges in phenotypic drug discovery: An industry perspective. *Nature reviews Drug discovery*. 16(8):531-543.
- Nicholas R. 2019. Pharmaceutical opioids in australia: A double-edged sword. National Centre for Education and Training on Addiction (NCETA), Flinders University, Adelaide.
- O'Brien DP, Comte E, Serafini M, Ehounou G, Antierens A, Vuagnat H, Christinet V, Hamani MD, Du Cros P. 2014. The urgent need for clinical, diagnostic, and operational research for management of buruli ulcer in africa. 14(5):435-440.
- O'Keefe ST, Kazeem H, Philpott RM, Playfer JR, Gosney M, Lye M. 1996. Gait disturbance in alzheimer's disease: A clinical study. *Age Ageing*. 25(4):313-316.
- Onozuka M, Watanabe K, Nagasaki S, Jiang Y, Ozono S, Nishiyama K, Kawase T, Karasawa N, Nagatsu I. 2000. Impairment of spatial memory and changes in astroglial responsiveness following loss of molar teeth in aged samp8 mice. *Behav Brain Res*. 108(2):145-155.
- Organization WH. 2012. Treatment of mycobacterium ulcerans disease (buruli ulcer): Guidance for health workers.
- Panza F, Lozupone M, Logroscino G, Imbimbo BP. 2019. A critical appraisal of amyloid- $\beta$ -targeting therapies for alzheimer disease. *Nature Reviews Neurology*. 15(2):73-88.
- Rosen WG, Mohs RC, Davis KL. 1984. A new rating scale for alzheimer's disease. *Am J Psychiatry*. 141(11):1356-1364.
- Royal MA. 2003. Botulinum toxins in pain management. *Physical Medicine and Rehabilitation Clinics*. 14(4):805-820.
- Salat K, Moniczewski A, Librowski T. 2013. Transient receptor potential channels-emerging novel drug targets for the treatment of pain. *Current medicinal chemistry*. 20(11):1409-1436.
- Sarfo FS, Le Chevalier F, Phillips RO, Amoako Y, Boneca IG, Lenormand P, Dosso M, Wansbrough-Jones M, Veyron-Churlet R, Guenin-Macé L. 2011. Mycolactone diffuses into the peripheral blood of buruli ulcer patients-implications for diagnosis and disease monitoring. *PLoS Negl Trop Dis*. 5(7):e1237.
- Sarfo FS, Phillips R, Wansbrough-Jones M, Simmonds RE. 2016. Recent



- advances: Role of mycolactone in the pathogenesis and monitoring of mycobacterium ulcerans infection/buruli ulcer disease. *Cellular microbiology*. 18(1):17-29.
- Sarfo FS, Phillips RO, Zhang J, Abass MK, Abotsi J, Amoako YA, Adu-Sarkodie Y, Robinson C, Wansbrough-Jones MH. 2014. Kinetics of mycolactone in human subcutaneous tissue during antibiotic therapy for mycobacterium ulcerans disease. *BMC infectious diseases*. 14(1):202.
- Sguilla FS, Tedesco AC, Bendhack LM. 2003. A membrane potential-sensitive dye for vascular smooth muscle cells assays. *Biochemical and biophysical research communications*. 301(1):113-118.
- Singhrao SK, Harding A, Simmons T, Robinson S, Kesavalu L, Crean S. 2014. Oral inflammation, tooth loss, risk factors, and association with progression of alzheimer's disease. *J Alzheimers Dis*. 42(3):723-737.
- Wan Y, Wallinder C, Plouffe B, Beaudry H, Mahalingam A, Wu X, Johansson B, Holm M, Botoros M, Karlén A. 2004. Design, synthesis, and biological evaluation of the first selective nonpeptide at2 receptor agonist. *Journal of medicinal chemistry*. 47(24):5995-6008.
- Willenborg M, Belz M, Schumacher K, Paufler A, Hatlapatka K, Rustenbeck I. 2012. Ca<sup>2+</sup>-dependent desensitization of insulin secretion by strong potassium depolarization. *American Journal of Physiology-Endocrinology and Metabolism*. 303(2):E223-E233.
- Wood JN. 2013. Results in analgesia—darwin 1, pharma 0. *New England Journal of Medicine*. 369(26):2558-2560.
- Woolf CJ. 2004. Pain: Moving from symptom control toward mechanism-specific pharmacologic management. *Annals of internal medicine*. 140(6):441-451.
- Xing Y, Zhang Y, Stabernack CR, Eger EI, Gray AT. 2003. The use of the potassium channel activator riluzole to test whether potassium channels mediate the capacity of isoflurane to produce immobility. *Anesthesia & Analgesia*. 97(4):1020-1024.
- Yekkirala AS, Roberson DP, Bean BP, Woolf CJ. 2017. Breaking barriers to novel analgesic drug development. *Nature reviews Drug discovery*. 16(8):545-564.
- Yotsu RR, Murase C, Sugawara M, Suzuki K, Nakanaga K, Ishii N, Asiedu K. 2015. Revisiting buruli ulcer. *The Journal of dermatology*. 42(11):1033-1041.
- Yu L, Shao C, Gao L. 2014. Developmental expression patterns for angiotensin receptors in mouse skin and brain. *Journal of the Renin-Angiotensin-Aldosterone System*. 15(2):139-149.

Zhang H, Han GW, Batyuk A, Ishchenko A, White KL, Patel N, Sadybekov A, Zamlynny B, Rudd MT, Hollenstein K. 2017. Structural basis for selectivity and diversity in angiotensin ii receptors. *Nature*. 544(7650):327-332.

# 국문 초록

## 병리학적 통증에 대한 마이코락톤의 진통효과 및 알츠하이머병에서의 삼차신경 운동 병리의 특성에 대한 연구

감각 및 운동 기능은 신체의 생리적 기능을 유지하는 데 중요한 역할을 한다. 신경학적 장애는 중추 및 말초 신경계에 영향을 미치며 일반적으로 이로 인해 나타나는 감각 및 운동 이상은 신경학적 다양한 증상을 유발할 수 있다. 이러한 증상들의 예로는 지각변화, 발작 및 혼란과 같은 정신적 증상과 마비, 운동능력 약화 및 협응력저하와 같은 기능 장애, 감각 이상 및 통증과 같은 감각장애로 나눌 수 있으며 이것을 이해하고 치료하는 것은 임상적으로 중요한 의미를 가진다. 따라서 본 학위 논문에서는 염증이나 신경 손상으로 인하여 발생하는 신경장애로 인하여 생기는 감각이상의 기전을 이

해하기 위하여 새로운 진통제 후보 물질인 mycolactone의 진통 효과를 검증하였다. Mycolactone은 *Mycobacterium ulcerans*에 의해 무통성 궤양을 일으키는 것으로 알려진 박테리아 유래 물질이다. 또한 신경퇴행성 질환에서의 말초감각 및 운동신경의 이상을 연구하기 위해 알츠하이머병의 모델인 5XFAD 마우스에서 안면영역으로 분포하는 뇌신경핵과 저작에 작용하는 근육을 조사하였다.

첫 번째 장에서는 mycolactone의 진통작용을 여러 통증 모델과 감각신경세포에서 연구하였다. 먼저 mycolactone의 진통 효과를 행동실험들을 통하여 조사하였을 때 신경병증과 염증성 통증 모델 마우스에서 기계적 통증 및 높은 온도로 인하여 발생하는 통증에서의 진통작용을 5 $\mu$ M 농도에서 확인하였다. 이러한 mycolactone의 진통 기전을 조사하기 위하여 Dorsal Root Ganglion (DRG) 감각신경세포에서 막전위 변화를 감지하는 염료를 기반으로 하는 세포분석법을 개발하였다. 본 실험을 통하여 세포독성이 없는 용량의 mycolactone이 AT2R을 통해 DRG 신경세포에서 과분극을 유도한다는 것을 증명했으며, 이러한 현상은 알려진 AT2R 리간드들에 의해 영향을 받지 않는 것을 확인하였다. 이러한 결과들은 DRG 신경세포에서 mycolactone의 AT2R 신호 전달 경로를 통한 과분극이 진통효과를

가져올 수 있음을 보여줌과 동시에 새로운 자연유래 진통제의 개발가능성을 보여준다.

두 번째 장에서는 5XFAD 알츠하이머 모델마우스에서 알츠하이머 병 환자들에게서 보이는 저작장애와 병리학적 특성을 평가하였다. 본 연구를 통하여 5XFAD 마우스에서 저작효율과 최대 교합력의 감소를 확인하였으나 일반적인 운동 기능에는 큰 변화가 없음을 확인하였다. 더욱이, 다른 저작 관련 신경핵들과 비교하였을 때 삼차운동신경핵(Vmo)에서 Amyloid- $\beta$  ( $A\beta$ )의 위치 특이적 축적과 활성이 증가한 미세교세포의 수 및 세포사멸이 관찰되었다. 또한 저작 관련 조직을 조직학적으로 분석한 결과 다른 안면 또는 설하 핵 신경이 분포하는 근육들에 비해 무게와 근섬유의 크기가 감소한 것을 확인하였다. 이러한 발견은 저작기능의 퇴화가 알츠하이머병의 진행에 관여할 수 있으며 저작기능의 조절이 알츠하이머병의 증상 조절에 잠재적으로 도움이 될 수 있음을 시사한다.

I 장과 II 장의 결과에 따르면 병리학 적 통증 (1 장)과 같은 신경 학적 장애에서 발견되는 말초 이상을 치료 표적으로 삼을 시, 박테리아 유래 물질의 잠재적 진통제로서의 사용가능성을 확인할 수 있다. 또한 알츠하이머 병과 같은 중추 신경 장애 (제 2 장)에 대한 본 연구의 결과는 알츠하이머

병에서 발견되는 삼차 운동계와 저작 기능 장애 발현 사이의 연관성을 제시하였다. 따라서 종합적으로 이 논문은 말초 및 중추 신경계 장애를 이해하는 것에 있어 말초 감각 운동 이상을 연구하는 것이 중요하다는 점을 시사한다.

---

주요어: 무통성 궤양; Mycolactone; AT2 수용체; DRG 감각신경세포; 막전위; 이미지 기반 세포분석; 통증; 알츠하이머병; 저작기능장애; 5XFAD

---

학번: 2014-22437